Towards the shear-wave sonic reverse time migration with the spectral element method

Mikhail Malovichko [a,*], Denis Sabitov [a], Maxim Dmitriev [b], Timur Zharnikov [a]

[a] *Aramco Innovations, Moscow, Russia*
[b] *EXPEC Advanced Research Center, Saudi Aramco, Dhahran, Saudi Arabia*

ARTICLE INFO

ABSTRACT

This paper evaluates feasibility of three-dimensional sonic reverse-time migration (RTM) based on the spectral element method (SEM). A GPU based algorithm capable of performing both fluid-solid and purely elastic RTM is presented. The key properties of our algorithm is efficient organization of GPU computations, use of optimized unstructured meshes and elements of high order, leveraged with sufficient amount of memory available on newer generations of GPUs. We review the imaging conditions (ICs) for shear-wave imaging, derive four ICs using the Lagrangian formalism and study their merits. We also propose a simple yet powerful approach for automatically constructing unstructured all-hexahedral meshes that respect the borehole geometry. The RTM algorithm's validity and merits are demonstrated through its application on synthetic data as well as a real data set. Overall, our results suggest that the sonic community already possesses the technical capability to perform industrial-scale sonic RTM, at least using GPU clusters employing top-tier chips with large global memory.

1. Introduction

Sonic logging plays a major role in determining formation properties. The physics of the waves emitted by a source in a fluid-filled borehole surrounded with (visco-) elastic medium is well understood Tang and Cheng (2004), Wang et al. (2020). A list of papers analysing various aspects of the acoustic field includes that based on semi-analytical solutions Cheng and Toksöz (1981), Schoenberg (1986), Schmitt (1988), the discrete wavenumber technique Meredith (1991), Byun and Toksöz (2006), and the finite-difference method Cheng et al. (1995), Cheng and Blanch (2008), Pissarenko et al. (2010), Tang et al. (2014), Wei and Tang (2012), Wang and Fehler (2017). Detailed descriptions of wave modes in different media and survey scenarios can be found in monographs Tang and Cheng (2004), Wang et al. (2020).

During the last three decades, much effort has been focused on the intriguing possibility of imaging deep structural features of the surrounding formations using full-waveform recording. The feasibility of creating deep images of near-borehole regions from full-waveform recordings was first demonstrated using P-wave reflections obtained with a monopole tool, see Hornby and Wiggins (1989), Hornby (1989) and many followup papers Fortin et al. (1991), Coates et al. (2000), Zhou et al. (2002), Tang (2004), Haldorsen (2005).

We are interested in shear wave imaging with a dipole tool. Development of this technology can be traced back at least to the 1980s Zemanek et al. (1986), Schmitt (1988). One of the earliest use of the dipole full-waveform record for reflection imaging was reported in Tang (2004). Dipole data exhibit strong directivity that allows resolving the azimuth ambiguity of single-well sonic data Tang (2004), Tang and Patterson (2009). Also, dipole data have good spatial resolution due to the reduced wavelength of the S-wave compared to the P-waves. Several more recent accounts on imaging dipole acoustic logs include Bolshakov et al. (2011), Tang et al. (2014), Hirabayashi et al. (2017), Hornby et al. (2018), Schmitt and Tonellot (2020), Alqatari et al. (2021), Hornby et al., 2024, Zhang et al. (2022), Li et al. (2020).

Although a variety of imaging methods has been applied to sonic data, such as the Radon transform Hornby (1989) and the $f - k$ transform, the Kirchhoff migration has gained particular attention in the sonic community, for example, Coates et al. (2000), Zhou et al. (2002), Tang and Patterson (2009), Bolshakov et al. (2011). Its variant, the equivalent-offset method, was promoted in Chabot et al. (2001), Zhang et al. (2009). The trial-reflector approach Hirabayashi (2016), Karpekin et al. (2019), Hirabayashi et al. (2022), proved to deliver highly satisfactory fracture images, can also be considered as a variant of the Kirchhoff migration. Despite the success, the Kirchhoff migration has

---

* Corresponding author.
E-mail address: mikhail.malovichko@aramcoinnovations.com (M. Malovichko).

limitations rooted in the ray approximation manifested by its inability to properly focus low-frequency wavelets and distinguish between the SS, PP and converted reflections, which are simultaneously present in dipole sonic data.

The reverse-time migration (RTM), which originated in the 1980th McMechan (1983), Baysal et al. (1983), was developed to address those limitations. The 3D acoustic RTM is routinely applied to surface seismic data, see review Zhou et al. (2018). The elastic RTM is less popular than the acoustic variant due to its high computational cost. Nevertheless, there is a whole body of literature devoted to various aspects of elastic imaging Sun and McMechan (1986), Chang and McMechan (1987), Sun and McMechan (2001), Yan and Sava (2008), Luo et al. (2009), Zhu et al. (2009), Luo et al. (2013), Feng and Schuster (2017), Sun et al. (2018).

The 2D acoustic RTM using the S-velocity distribution has been applied to dipole sonic data in Schmitt and Tonellot (2020), Alqatari et al. (2021). While being one of the most massive RTM applications for field data, those studies highlighted the inability of acoustic solvers properly explain the complex interaction between fluid and solid, resulting in noisy images.

The fluid-solid RTM of sonic data was proposed in Li et al. (2013a, 2013b, 2014). Those authors implemented the 2D finite-difference (FD) RTM and applied it to image P-reflections of the monopole field data. The same authors expanded their approach into the 3D fluid-solid RTM Li et al. (2016, 2019). The 3D fluid-solid RTM based on the FD approach was applied to synthetic dipole data in Gong et al. (2015, 2016, 2018). The finite difference method has a long history of applications in sonic simulation. We refer to Cheng et al. (1995), Cheng and Blanch (2008), Wei and Tang (2012), Wang et al. (2020)(Appendix B) for details. Recent applications of the FD method to sonic RTM can be found in Grohmann et al. (2024), Li et al. (2024). The FD schemes produce highly accurate simulations but may encounter challenges due to their reliance on structured meshes. The staircase approximation of the borehole, small Courant number in fluid, and limitation on the accuracy order increase the size of the computational grid, making such computations heavy.

The spectral-element method (SEM) has gained significant attention due to its unique combination of geometric flexibility from the finite-element method (FEM) and high computational efficiency. It has been studied by many authors, Komatitsch and Vilotte (1998), Komatitsch and Tromp (1999), Komatitsch et al. (2000), Chaljub et al. (2003), Festa and Vilotte (2005), Peter et al. (2011). The fluid-solid SEM-based RTM for marine seismology was reported in Luo et al. (2013). The SEM seems to be the ideal match for the sonic imaging of open boreholes in fast formations at frequencies below approx. 5 kHz. Still, only a few references are dedicated to the sonic simulation by SEM, Ponomarenko et al. (2020), Bazulin et al. (2021).

The full-wave elastic sonic RTM has long remained unreachable due to the huge computational demands it imposes. Nevertheless, the new generation of GPUs brings the community close to industrial applications of elastic sonic RTM. The key factors that have made such computations possible include the steady growth of global GPU memory across several hardware generations and a sufficiently sized shared memory, combined with appropriate software design, such as optimized mesh generation, implementation of high-order elements, and the avoidance of multi-GPU communication Section 6.

The primary objective of this study is to evaluate the feasibility of elastic and fluid-solid RTM of sonic data. We present the two variant of the three-dimensional SEM-based RTM algorithms: purely elastic and solid-fluid. We review the imaging conditions targeting the shear-wave imaging, present a rigour and simple derivation using the Lagrangian formalism and test their performance. An effective approach for automatically constructing unstructured all-hexahedral meshes that accurately capture the borehole geometry is proposed. We discuss the most critical aspect of our algorithm: the GPU kernel that performs tensor reduction between stiffness tensor and local degrees of freedom (DOFs).

Numerical experiments with a model used in H. Wang et al. (2020) (Chapter 7) are presented. Based on our numerical experiments conducted on a previous generation of GPUs, we contend that the sonic community already possesses the technical capability to perform industrial-scale sonic RTM with GPU clusters employing newer chips.

The paper is organized as follows. Section 2 provides an overview of the cross-dipole survey, covering general information. Section 3 focuses on modelling using the SEM. Section 4 discusses mesh generation techniques. Section 5 reviews imaging conditions. Section 6 presents the results of numerical experiments. Section 7 presents tests involving real data set. Section 8 discusses properties of sonic SEM RTM from the geophysical prospective. Section 9 contains concluding remarks. Appendix A provides details about our GPU implementation.

2. Cross-dipole survey

In this section, we briefly review those aspects of cross-dipole surveys that are essential for RTM. The acoustic pulse is initiated by one of the two dipole transmitters. One possible design is shown in Fig. 1: each dipole transmitter has two elements with opposite azimuths. During excitation, the elements emit positive and negative compressional waves. The combined action of these waves on the borehole walls (the source "dipole") generates compressional and shear converted waves in the rocks, as well as guided modes (mostly flexural waves, but also remnant Stoneley waves due to non-ideal tool centring). Receiving elements at each Z-level record pressure, which can be combined into the two principal data sets corresponding to the receiver "dipoles". These principal components are usually referred to as XX, YY, XY, and YX.

The guided modes travelling along the borehole dominate reflections by several orders of magnitude and have complicated patterns dependent on borehole diameter, source frequency, mud and rocks parameters - see Tang and Cheng (2004), Cheng and Blanch (2008), Wang et al. (2020). For deep imaging, that part of the signal can be safely removed from the data. The remaining data still present a complicated mix of P-/ S- and converted waves, reflected and refracted.

Shear body waves in isotropic medium can be split into two components: one polarised in the vertical plane (SV mode) and horizontal plane (SH mode), see Fig. 2. A simple but frequently used model based
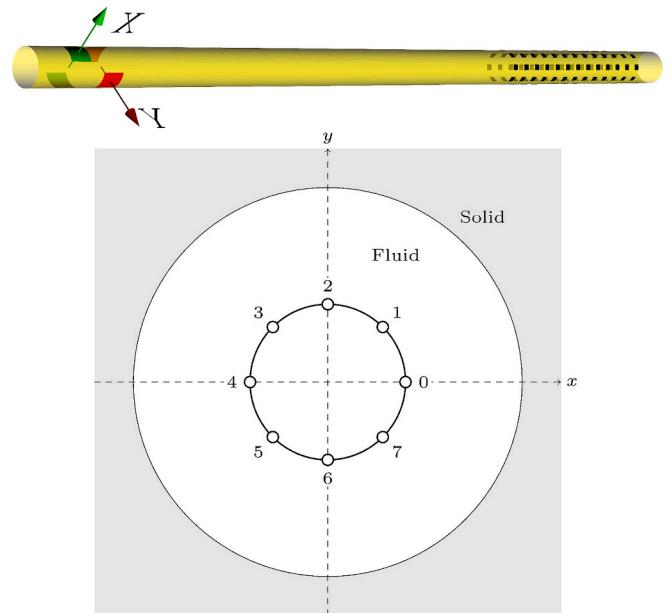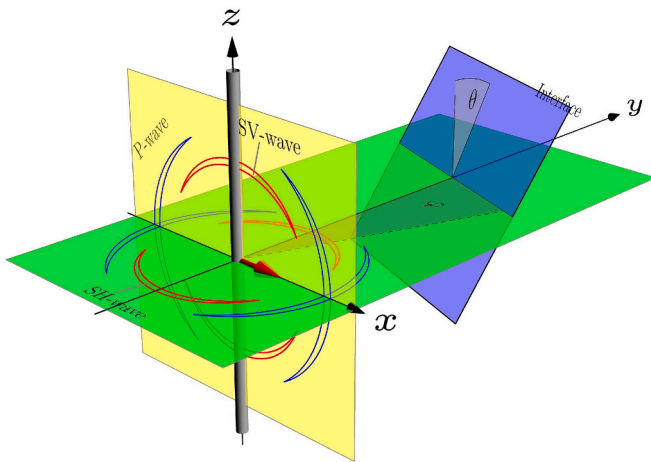

Fig. 1. The geometry of a cross-dipole sonic survey. (a) Schematic representation of the tool with two orthogonal dipole transmitting systems (X and Y) and several circular arrays of receivers. (b) Sketch of a circular array consisting of 8 receiving elements.

Fig. 2. Schematic geometry of a cross-dipole sonic survey. Note that, the S- and SH-waves depicted are actually converted waves generated at the walls of the fluid column.

on the low-frequency far-field dipole approximation neglecting the borehole effect Tang and Patterson (2009), Tang et al. (2009) predicts the following composition of the recorded data,

$$
\begin{aligned}
XX &= SH\cos^2\varphi + SV\sin^2\varphi, \\
YY &= SH\sin^2\varphi + SV\cos^2\varphi, \\
XY &= YX = (SV - SH)\cos\varphi\sin\varphi,
\end{aligned}
\tag{1}
$$

where φ is the reflector strike angle (Fig. 2). It suggests an equal contribution from the two modes. However, a more accurate model considering borehole and dipping angle θ Tang et al. (2014) explains why the SH dominates real data sets and constitutes the principal modality in dipole shear-wave surveys. The SV mode is important when the dipole is oriented towards a dipping reflector, but this configuration also generates P—S and S—P waves spoiling the image.

The pre-processing steps for cross-dipole sonic data may vary depending on the application, but a fundamental procedure is extracting the dipole mode. The following formula computes the dipole mode for each i-th circular array,

$$
d_i(t) = \sum_{k=0}^{7} d_{i,k}(t)\cos\left(\frac{2\pi k}{8} - \alpha\right),
\tag{2}
$$

where α is a predefined direction. Usually, α takes either 0 or $\pi/2$, so it gives the four data sets XX, XY, YX, and YY. This procedure suppresses symmetric pressure oscillations with respect to the azimuth (monopole modes) and boosts anti-symmetric oscillations (dipole modes). Identification of azimuth of reflectors is a separate task, which we do not consider here, see Tang et al. (2009), Bolshakov et al. (2011), Hirabayashi et al. (2017).

We emphasise that, after the dipole mode extraction, reflected waveforms still cannot be fully described using solid simulation alone. First, the visible spectrum will be shifted towards higher frequencies due to significant attenuation of low frequencies in the waves travelled in the system borehole-solid-borehole. Second, recorded reflections contain strong ringing caused by reverberation inside the borehole - a short pulse turns into a long wave packet in the geological medium (Fig. 3). In addition, the data still retain residual monopole modes.

3. Fluid-solid forward modelling

For the sonic simulation, we solve the coupled fluid-solid system of partial differential equations (PDEs). Only a short section of the borehole is included in the sonic modelling at a time, so the fluid can be considered homogeneous. We follow the self-adjoint formulation of
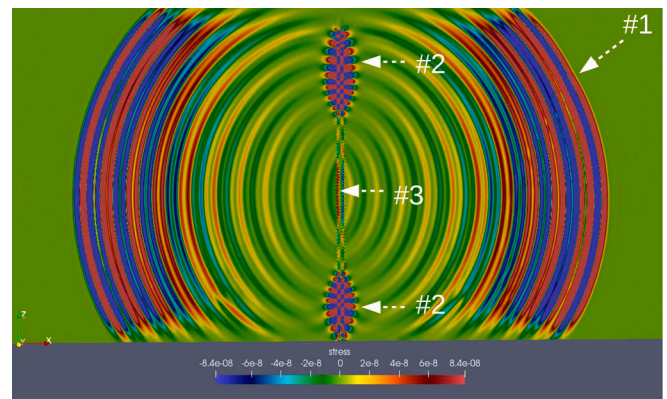
Fig. 3. A typical fluid-solid simulation highlighting reverberations caused by a fluid-filled borehole: #1 is the outgoing wave train (primary converted waves), #2 are guided modes, #3 are trapped waves causing remnant ringing in the fluid persistent during the entire simulation.

Komatitsch et al. (2000). The fluid is parameterised with sound velocity c and a constant density ρ_f. The motion in the fluid part is described with the scalar velocity potential φ that relates to the particle velocity $\dot{\boldsymbol{u}}$ and pressure p as follows Landau and Lifshitz (1959),

$$
\dot{\boldsymbol{u}} = \nabla\varphi, \quad p = -\rho_f\dot{\varphi}.
\tag{3}
$$

We assume a linear isotropic solid. It is characterized with density ρ, and Lamé parameters λ and μ. The constitutive relation is given by

$$
\begin{aligned}
\widehat{\sigma} &= \widehat{C} : \widehat{\varepsilon}, \\
\widehat{\varepsilon} &= \left(\nabla\boldsymbol{u} + \nabla\boldsymbol{u}^T\right)/2
\end{aligned}
\tag{4}
$$

where $\widehat{\varepsilon}$ is a 2-rank strain, $\boldsymbol{u}$ is displacement, $\widehat{C}$ is a 4-rank tensor given by

$$
C_{ijkl} = \lambda\delta_{ij}\delta_{kl} + \mu\left(\delta_{ik}\delta_{jl} + \delta_{il}\delta_{jk}\right),
\tag{5}
$$

with δ_{ij} stands for the Kronecker delta. The strong form of equations of motion reads,

$$
\begin{aligned}
\rho\ddot{\boldsymbol{u}} - \operatorname{div}\widehat{\sigma} &= \boldsymbol{f}, \quad \text{in solid,} \\
\beta\ddot{\varphi} - \Delta\varphi &= s, \quad \text{in fluid,}
\end{aligned}
\tag{6}
$$

where $\boldsymbol{f}$ and s are the forcing terms is solid and fluid, respectively; $\beta = c^{-2}$. Absorbing layers are omitted in eqs. (6) to simplify formulas. In the programming implementation, so-called sponge layers are added to the sides of the computational domain.

At the solid-fluid interface continuity of traction and the normal velocity must be satisfied,

$$
\begin{aligned}
\widehat{\sigma}\cdot\boldsymbol{n} &= \rho_f\dot{\varphi}\boldsymbol{n}, \quad \text{in solid,} \\
\nabla\varphi\cdot\boldsymbol{n} &= \dot{\boldsymbol{u}}\cdot\boldsymbol{n}, \quad \text{in fluid.}
\end{aligned}
\tag{7}
$$

The system of PDEs is complemented by the boundary conditions at the outer boundary,

$$
\begin{aligned}
\widehat{\sigma}\cdot\boldsymbol{n} &= 0, \quad \text{at solid outer boundary,} \\
\varphi &= 0, \quad \text{at fluid outer boundary.}
\end{aligned}
\tag{8}
$$

The initial conditions are zero,

$$
\boldsymbol{u} = \dot{\boldsymbol{u}} = 0, \quad \varphi = \dot{\varphi} = 0 \quad \text{at } t = 0.
\tag{9}
$$

Now we formulate the weak form of problem (6), (7),(8),(9). In RTM practice, it is typical to assume that the coefficients ρ, λ, and μ are smooth. It greatly simplifies the choice of the function spaces. We define a space of functions from interval $[0, T]$ to displacement,

$$
\mathscr{U} := \left\{ \boldsymbol{q} = [0, T] \mapsto H^1(V_s)^3 : \left(\int_0^T \|\boldsymbol{q}\|_{H^1}^2\, dt\right)^{1/2} < \infty \right\},
\tag{10}
$$

where H^1 is the standard notation for a Sobolev space of functions having a square-integrable weak gradient. Similarly we define the space of functions from $[0, T]$ to fluid potential,

$$\mathscr{F} := \left\{ q = [0, T] \mapsto H^1\left(V_f\right) : \left(\int_0^T \|q\|_{H^1}^2 \, dt \right)^{1/2} < \infty \right\}. \quad (11)$$

We seek a pair of functions $\boldsymbol{u} \in \mathscr{U}$ and $\varphi \in \mathscr{F}$ such that

$$\int_{V_s} \rho \ddot{\boldsymbol{u}} \cdot \widetilde{\boldsymbol{u}} \, dx + \int_{V_s} \nabla \boldsymbol{u} : \widehat{C} : \nabla \widetilde{\boldsymbol{u}} \, dx =$$
$$- \int_{\Gamma_{fs}} (\rho_f \dot{\varphi} \boldsymbol{n}) \cdot \widetilde{\boldsymbol{u}} \, dx + \int_{V_s} \boldsymbol{f} \cdot \widetilde{\boldsymbol{u}} \, dx, \quad \forall \widetilde{\boldsymbol{u}} \in \mathscr{U},$$
$$\int_{V_f} \beta \varphi \widetilde{\varphi} \, dx + \int_{V_f} \nabla \varphi \cdot \nabla \widetilde{\varphi} \, dx = \quad (12)$$
$$- \int_{\Gamma_{fs}} (\dot{\boldsymbol{u}} \cdot \boldsymbol{n}) \widetilde{\varphi} \, dx + \int_{V_f} s \widetilde{\varphi} \, dx, \quad \forall \widetilde{\varphi} \in \mathscr{F}.$$

Here tilde ~ over a variable denotes the test function.

We use the SEM to solve system (12) numerically. The SEM has been extensively studied in the context of linear fluid-solid wave equations, e. g. Komatitsch and Tromp (1999), Komatitsch et al. (2000), Chaljub et al. (2003), Festa and Vilotte (2005), among many others. Therefore, a detailed discussion of this aspect will be omitted. In this study, we employed an in-house C++ implementation based on CUDA. A typical fluid-solid simulation is presented in Fig. 3.

3.1. Computational strategy of sonic RTM

In this section, we address design choices to enhance the efficiency of SEM-based 3D sonic RTM.

Sonic data, characterized by a narrow aperture and few number of channels, permit individual processing of each shot with a small computational mesh. Our software generates a small computational mesh with surrounding absorbing layers for each shot.

Sonic datasets often entail a significant number of shots, sometimes tens of thousands or more. Given the narrow aperture, the most efficient parallelization approach is to refrain from sharing individual forward and adjoint simulations across multiple GPUs. This improves coarse-grained parallelism and significantly reduces overall runtime. The primary constraint is the available global memory on GPU cards.

In elastic 3D RTM, the total number of degrees of freedom (DOFs) plays a vital role. We recommend using unstructured meshes with higher-order elements to minimize the total element count and maximize the proportion of internal DOFs within an element. In our computations we use the 7-th order.

The computational mesh can rapidly expand when a borehole cross-section is discretized with many elements. Currently, we do not consider data at frequencies above 3–7 kHz. However, as soon size of elements in the fluid exceed the borehole diameter, high-order isoparameteric element are able to describe the borehole geometry with great accuracy.

The most substantial computational challenge arises with a small-diameter borehole in high-velocity rock. In such cases, the required memory can easily exceed the available global memory. While a multi-GPU approach can theoretically address this issue, it becomes impractical for a large number of data shots due to performance degradation.

4. Mesh generation

Mesh generation is a crucial aspect of SEM-based RTM. The SEM should be implemented on hexahedral meshes for efficiency. At the same time, the small borehole diameter and high S-wave velocities in the surrounding medium impose high requirements on mesh quality: it should be unstructured, containing small elements near the borehole and larger elements in the remaining region. Finding an efficient

algorithm to generate a general unstructured all-hexahedral mesh remains a challenge, despite being a long-standing focus of research in this field, see recent review Pietroni et al. (2022). Several advanced algorithms are available in commercial specialised packages like CUBIT.

We propose a simpler approach based on the relative simplicity of our model. A mesh consists of the borehole with fluid and the surrounding elastic medium. We consider a scenario where the wavelength in the fluid is much larger than the borehole diameter. Simulations have shown that 7-th order discretization requires at least one element per wavelength Ponomarenko et al. (2020). Our meshing algorithm starts with describing the borehole by stacking cylindrical elements. Their horizontal diameter is equal to that of the borehole, while the fluid's wavelength determines the vertical size. The elements far from the borehole are determined solely by the S-wave velocity in the medium. Ideally, these elements are parallelepipeds of the maximum size allowed for that wavelength.

The main challenge lies in constructing transitional elements between the central cylindrical elements and the larger outer parallelepiped elements. The radial coarsening rate is flexible, achieved through transitional rings (Fig. 4(a)-(c)) and their combinations. In contrast, the coarsening rate in the vertical direction is restricted to the two patterns (3:1 and 2:1, as shown in Fig. 4(d), (e)). For instance, the height of the bore elements, H, after coarsening with the 2:1 template turns into 2H, which might exceed the S-wave wavelength. In such cases, we reduce the element height within the borehole. There is a limit to this reduction: the cylindrical elements should not have a height-to-width ratio smaller than 1, as it would decrease the Courant number for the entire mesh. Fig. 6 illustrates different combinations of parameters (borehole diameter and S-wave wavelength in the external medium, normalised by the wavelength in the fluid) and their impact on the coarsening strategy. An example of the mesh is provided in Fig. 5.

5. Adjoint problem and imaging conditions

The adjoint problem and the imaging conditions (ICs) for the elastic RTM have been extensively discussed in the literature, so we present a brief overview for completeness.

The coupled displacement formulation with homogeneous fluid is self-adjoint, simplifying theory and programming implementation. The derivation based on the variational approach targeting the SEM discretisation has been presented in Liu and Tromp (2006) and cited in many papers since then Zhu et al. (2009), Luo et al. (2013). In principle, adding the fluid into the system does not pose difficulties as soon as the system of coupled PDEs remains self-adjoint, as in Komatitsch et al. (2000), where the wave equation in the fluid is formulated for the
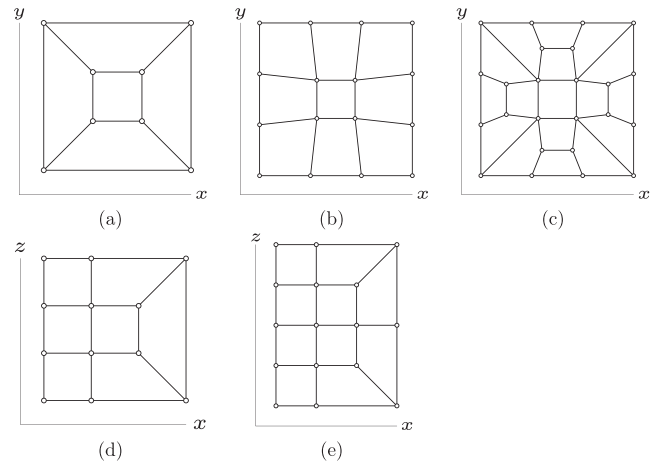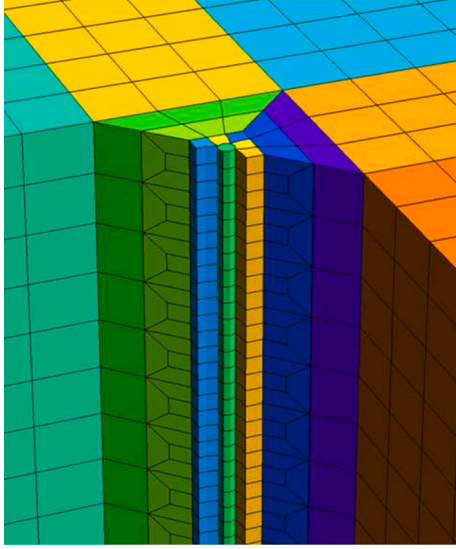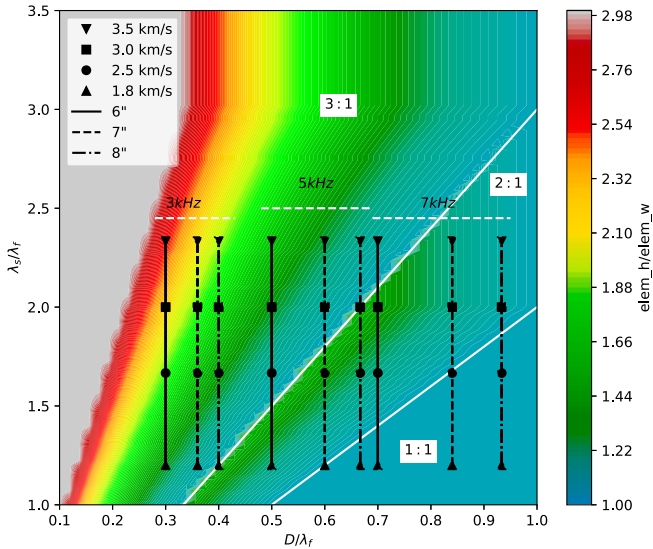

Fig. 4. Several coarsening templates. Radial coarsening: (a)-(c). Vertical coarsening: (d) 3:1, (e) 2:1.

Fig. 5. Example of an all-hexahedral unstructured mesh. The central elements are rendered as prisms with straight faces, but they are actually curved to a cylindrical shape.

Fig. 6. Meshing strategy selection based on normalised borehole diameter (D/λ_f) and normalised S-wave wavelength (λ_s/λ_f). The borehole diameter (D) and S-wave wavelength (λ_s) are normalised by the fluid wavelength (λ_f). The labels "3:1", "2:1", and "1:1" indicate what coarsening algorithm is available. The height of the borehole elements is limited by either λ_f or λ_s through the coarsening algorithm. The colour scale represents the highest height-to-width ratio achievable in a borehole. Reference points for different combinations of frequencies, S-wave velocities, and borehole diameters are plotted on top of the figure (see legend).

velocity potential. However, non-self-adjoint systems have been discretised by the SEM in literature. For example, Peter et al. (2011) advocate for the fluid displacement potential, which results in the not self-adjoint formulation. In such a case, attention should be paid to the adjoint formulation Cao et al. (2021).

The ICs can be viewed as the variation of the misfit functional with respect to the model parameters, see Liu and Tromp (2006). On the other hand, the curl IC is usually derived from the Helmholtz decomposition, followed by Claerbout's imaging principle of the zero-lag cross-correlation between forward and adjoint wavefields Wang et al. (2017). We

will show that the curl IC can be obtained from the same variational principle.

Let $d_i(t)$ be a full-waveform pressure recording registered by the i-th receiver. Formally, it is defined through the observation operator Q_i as follows,

$$d_i(t) = Q_i\varphi := -\rho_f \int_V \dot{\varphi}(\boldsymbol{x},t)\delta(\boldsymbol{x}-\boldsymbol{x}_i)\,d\boldsymbol{x}, \tag{13}$$

where $\delta(\boldsymbol{x})$ is the Dirac delta, $\boldsymbol{x}_i$ be a coordinate of the i-th receiver. We keep this notation for a while, but later we consider a more complicated case involving a weighted sum of data traces.

Let Φ be the data misfit,

$$\Phi := \frac{1}{2}\int_V \sum_{i=1}^{N}(d_i(t) - Q_i\varphi)^2\,dt \tag{14}$$

We formulate the RTM as the following optimization problem,

$$\underset{\mu,\lambda,\rho}{\text{minimize}} \quad \Phi, \text{subject to}\left(6\right),\left(7\right),\left(8\right),\left(9\right). \tag{15}$$

Let us form the Lagrangian,

$$\mathscr{L}(\boldsymbol{u},\boldsymbol{w},\varphi,\psi,\mu,\lambda,\rho) :=$$
$$\Phi + \int_0^T \int_{V_s}(\rho\ddot{\boldsymbol{u}} - div(\widehat{C}:\widehat{\varepsilon}) - \boldsymbol{f})\cdot\boldsymbol{w}\,d\boldsymbol{x}\,dt$$
$$+ \int_0^T \int_{V_f}(\beta\ddot{\varphi} - \Delta\varphi - s)\psi\,d\boldsymbol{x}\,dt. \tag{16}$$

Functions $\boldsymbol{w}(x,t)$ and $\psi(x,t)$ are Lagrange multipliers, which we also call the adjoint displacement and adjoint potential, respectively. We seek functions $\boldsymbol{u}(x,t)$, $\boldsymbol{w}(x,t)$, $\varphi(x,t)$, $\psi(x,t)$, $\mu(x)$, $\lambda(x)$, and $\rho(x)$, such that they give the saddle point to the Lagrangian,

$$\begin{aligned}(\nabla_u\mathscr{L}\widetilde{\boldsymbol{u}}) &= 0, \; \forall\widetilde{\boldsymbol{u}}, & (\nabla_w\mathscr{L}\widetilde{\boldsymbol{w}}) &= 0, \; \forall\widetilde{\boldsymbol{w}}, \\ (\nabla_\varphi\mathscr{L}\widetilde{\varphi}) &= 0, \; \forall\widetilde{\varphi}, & (\nabla_\psi\mathscr{L}\widetilde{\psi}) &= 0, \; \forall\widetilde{\psi}, \\ (\nabla_\mu\mathscr{L}\widetilde{\mu}) &= 0, \; \forall\widetilde{\mu}, & \left(\nabla_\lambda\mathscr{L}\widetilde{\lambda}\right) &= 0, \; \forall\widetilde{\lambda}, \\ (\nabla_\rho\mathscr{L}\widetilde{\rho}) &= 0, \; \forall\widetilde{\rho}, \end{aligned} \tag{17}$$

and satisfy conditions (7), (8), (9). Here notation $\nabla_x\mathscr{L}$ means the derivative of $\mathscr{L}$ with respect to x, $(\cdot,\cdot)$ means the scalar product in an appropriate function space.

Integrating by parts, we verify

$$(\nabla_\varphi\mathscr{L},\widetilde{\varphi}) =$$
$$-\int_0^T \int_{V_f}\left[\sum_{i=1}^{N}Q_i^*(d_i - Q_i\varphi)\right]\widetilde{\varphi}\,d\boldsymbol{x}\,dt +$$
$$\int_0^T \int_{V_f}(\beta\ddot{\psi} - \Delta\psi)\widetilde{\varphi}\,d\boldsymbol{x}\,dt = 0, \quad \forall\widetilde{\varphi}. \tag{18}$$

We set $\varphi = \dot{\varphi} = 0$ at $t = T$ during the time integration. This variational equality corresponds to the following strong formulation,

$$\beta\ddot{\psi} - \Delta\psi = \sum_{i=1}^{N}Q_i^*(d_i - Q_i\varphi), \quad \text{in } V_f \tag{19}$$

$$\psi = \dot{\psi} = 0 \text{ at } t = T, \quad \psi = 0 \text{ on } \Gamma_f.$$

In RTM practice, it is common to put $Q_i^* d_i$ instead of $Q_i^*(d_i - Q\varphi)$. We can further simplify it by dropping the time derivative in the definition of Q^*, which results in a half-cycle shift of the recorded wavelets but removes the need to differentiate noisy data (see Section 6.4).

Similarly, from $(\nabla_u\mathscr{L}\widetilde{\boldsymbol{u}}) = 0$ we get

$$\rho\ddot{\boldsymbol{w}} - div(\widehat{C}:\nabla\boldsymbol{w}) = 0 \quad \text{in } V_s, \tag{20}$$
$$\boldsymbol{w} = \dot{\boldsymbol{w}} = 0 \text{ at } t = T, \quad \boldsymbol{w} = 0 \text{ at } \Gamma_s.$$

The interface condition couples adjoint displacement $\boldsymbol{w}$ and adjoint potential ψ, exactly as was specified in (7).
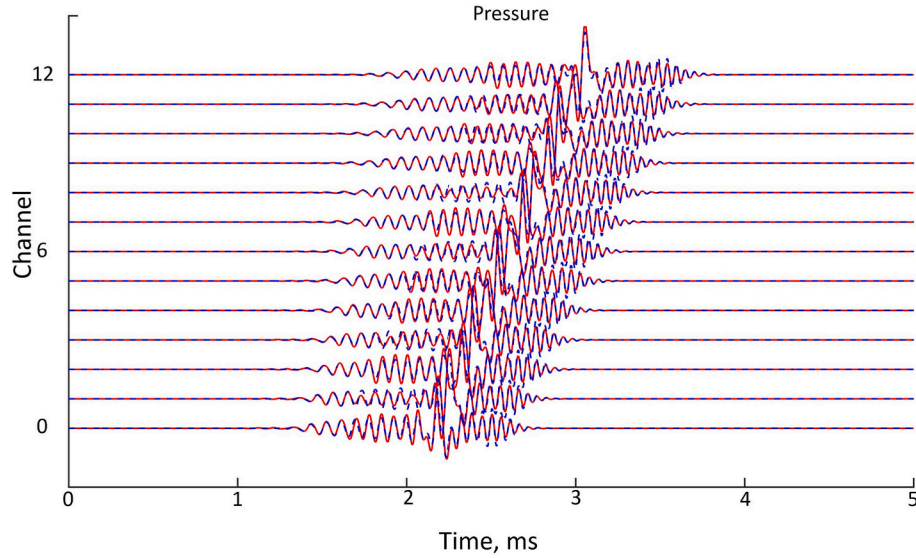
Fig. 7. Validation of the numerical solver. The red lines are numerical pressure at receivers (13 channels), the blue line represents analytical solution. (For interpretation of the references to colour in this figure legend, the reader is referred to the web version of this article.)

Table 1
Material properties.

	ρ, kg/m^3	V_p, m/s	V_s, m/s
Water	1000	1500	
Material 1	2600	3048	1894
Material 2	2400	3390	1996

Applying the same technique to condition $(\nabla_w \mathscr{L}, \widetilde{w}) = 0$ and $(\nabla_\psi \mathscr{L}, \widetilde{\psi}) = 0$ we recover the forward problem (6),(8),(9).

Now we discuss the imaging conditions. From variational equality we see

$$(\nabla_\rho \mathscr{L} \widetilde{\rho}) = \int_{V_s} \left[\int_0^T \ddot{u} \cdot w \, dt \right] \widetilde{\rho} \, dx = 0, \quad \forall \widetilde{\rho}. \tag{21}$$

The dot product $(\cdot, \cdot)$ for functions independent of time includes only space integration. We conclude that (21) corresponds to the following formulation,

$$I_\rho := \nabla_\rho \mathscr{L} = \int_0^T \ddot{u} \cdot w \, dt = -\int_0^T \dot{u} \cdot \dot{w} \, dt. \tag{22}$$

The last equality follows from integration by parts.

Let's consider variational inequality with respect to Lamé parameters. We have

$$\left(\nabla_\lambda \mathscr{L} \widetilde{\lambda} \right) = -\int_{V_s} \left[\int_0^T \nabla w : \delta_{ij} \delta_{kl} : \nabla u \, dt \right] \widetilde{\lambda} \, dx = 0, \quad \forall \widetilde{\lambda}. \tag{23}$$

and, thus,

$$I_\lambda := \nabla_\lambda \mathscr{L} = \int_0^T \nabla w : \delta_{ij} \delta_{kl} : \nabla u \, dt = \int_0^T \text{div} u \, \text{div} w \, dt. \tag{24}$$

We also have

$$(\nabla_\mu \mathscr{L} \widetilde{\mu}) = \int_{V_s} \left[\int_0^T \nabla w : \left(\delta_{ik} \delta_{jl} + \delta_{il} \delta_{jk} \right) : \nabla u \, dt \right] \widetilde{\mu} \, dx = 0, \forall \widetilde{\mu}, \tag{25}$$

and

$$I_\mu := \nabla_\mu \mathscr{L} = \int_0^T \nabla w : \left(\delta_{ik} \delta_{jl} + \delta_{il} \delta_{jk} \right) : \nabla u \, dt = \int_0^T \widehat{\widetilde{\xi}} : \widehat{\varepsilon} \, dt, \tag{26}$$

where ξ is the adjoint strain defined as in (5).

Sometimes it is useful to employ another parametrisation of $\widehat{C}$,

$$C_{ijkl} = (\kappa - 2/3\mu)\delta_{ij}\delta_{kl} + \mu\left(\delta_{ik}\delta_{jl} + \delta_{il}\delta_{jk}\right). \tag{27}$$

In that case,

$$I'_\mu := \int_0^T \nabla w : \left(-2\big/3\mu\delta_{ij}\delta_{kl} + \delta_{ik}\delta_{jl} + \delta_{il}\delta_{jk} \right) : \nabla u \, dt = \int_0^T \text{Dev}\,\widehat{\widetilde{\xi}} : \text{Dev}\,\widehat{\varepsilon} \, dt, \tag{28}$$

where Dev is the deviatoric part of strain,

$$\text{Dev}\,\widehat{\varepsilon} = \varepsilon_{ij} - (1/3)\,\varepsilon_{kk}\delta_{ij}. \tag{29}$$

The last equality in (28) can be verified directly.

Finally, we show that the curl-curl IC can be obtained as follows,

$$I''_\mu := \int_0^T \nabla w : \left(\delta_{ik}\delta_{jl} - \delta_{il}\delta_{jk} \right) : \nabla u \, dt = \int_0^T \text{curl}\,u \cdot \text{curl}\,w \, dt. \tag{30}$$

To prove the last equality, we recall the epsilon-delta equality,

$$\varepsilon_{ijk}\varepsilon_{kpq} = \delta_{ip}\delta_{jq} - \delta_{iq}\delta_{jp}, \tag{31}$$

where ε_{ijk} is the Levi-Civita symbol, δ_{ij} is the Kronecker delta. With the use of the Einstein summation, we have

$$\begin{aligned}
&\left(\partial_i u_j \right)\left(\delta_{ip}\delta_{jq} - \delta_{iq}\delta_{jp} \right)\left(\partial_p w_q \right) = \\
&\left(\partial_i u_j \right)\left(\varepsilon_{ijk}\varepsilon_{kpq} \right)\left(\partial_p w_q \right) = \\
&\left(\partial_i u_j \varepsilon_{ijk} \right)\left(\varepsilon_{kpq}\partial_p w_q \right) = \\
&\left(\text{curl}\,u \right)_k \left(\text{curl}\,w \right)_k.
\end{aligned} \tag{32}$$

The last equality in this chain follows from the definition of curl.

Our GPU implementation is discussed in Appendix A.
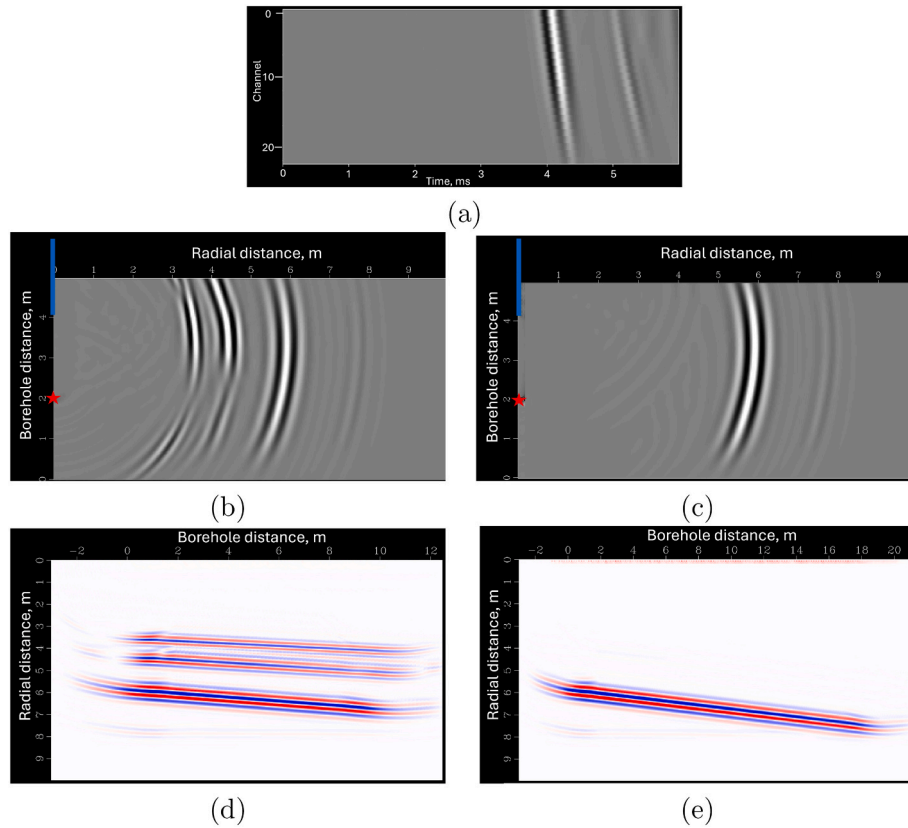
Fig. 8. Test 1. Comparison of I_ρ and I_λ: (a) synthetic data shot showing the P- and PS-reflections; (b) shot obtained with I_ρ; (c) shot obtained with I_λ; (d) 128 shots obtained with I_ρ; (e) 128 shots obtained with I_λ. The red star and blue line mark location of the source and receivers, respectively. In Panel (d), two of the three shallow interfaces are artifacts, while only the true interface is visible in Panel (e). (For interpretation of the references to colour in this figure legend, the reader is referred to the web version of this article.)

6. Numerical experiments

In this section, we evaluate our RTM algorithm on synthetic data. The section is not intended to analyze geophysical aspects of sonic RTM such as space resolution etc., but to provide a validation test for our software. At the same time, the examples have been chosen to highlight on specific aspects of the full-waveform sonic RTM.

The computations in this section were performed using Quadro 5000 cards with a compute capability of 6 and 16 GB of memory. It's worth noting that newer generation chips with compute capability 7,8 and 9 offer a substantial increase in memory capacity.

We validated our forward modelling engine by repeated tests presented in Zharnikov et al. (2021), Bazulin et al. (2021). Additionally, we performed testing against analytical solution by Plyushenkov and Turchaninov (2006), as presented below. The peculiarity of the latter solution is that it always simulates sonic tool by including a small cylinder in the center of the borehole with zero Dirichlet BCs. To replicate this behavior in our solver, we removed cylindrical elements from the center of the 3D mesh and applied zero Dirichlet BCs there. The resulting model consisted of a central empty cylinder (radius = 0.05 m), a fluid-filled borehole (radius = 0.10 m), and elastic solid surrounding it. The fluid properties were set to Vp=1500 m/s and ρ=2000 kg/m^3. The solid parameters were ρ=2640 kg/m^3, Vp=3901 m/s, and Vs=2682 m/s. A monopole ring transmitter was located at a radius of 0.05 m. Thirteen receivers were placed at a radius of 0.055 m. The distance between the source and the first receiver was 2.8448 m, with the rest of the receivers, spaced 0.1016 m apart. We observe (Fig. 7) a good match between the SEM and analytical solution. The minor discrepancies are attributed to the reflections from the walls of the computational domain.

In what follows, we used a simple model consisting of a flat interface

between two elastic materials because a similar model was used earlier for sonic migration evaluation Wang et al. (2020) (Chapter 7). Material parameters are listed in Table 1. We consider three imaging cases: elastic data — elastic migration(ED-EM), fluid-solid data — elastic migration (FSD-EM), and fluid-solid data — fluid-solid migration (FSD-FSM). The ED-EM experiments deviate significantly from practical cases since the presence of a borehole profoundly impacts the wavefield, not to mention the different mechanisms of the source and receivers. However, it is an essential initial step in gaining insights into sonic RTM. The FSD-EM is a realistic scenario when one tries to image real data with a purely elastic RTM engine. The FSD-FSM case is computationally heavy but can capture the fluid-solid interaction.

6.1. Test1: I_λ and I_ρ imaging conditions

As was outlined before, the SH waves constitute the principal modality of the dipole sonic data. Still, we want to examine I_λ and I_ρ ICs for completeness. To generate considerable P-wave response, we placed the interface almost perpendicular to the X-axis with $\varphi = 90\,deg$ and $\theta = 6\,deg$ and computed the difference between seismograms with and without the interfaces. The calculation was performed with a tool with of 22 circular arrays of receivers separated 0.1016 m apart; the distance between the source and the first receiver was 2.1336 m. The tool step size was 0.15 m. The source emitted the 3 kHz Ricker wavelet (Fig. 8).

The modelling and the RTM employed the elastic solver, with the source represented as an X-force and the receivers recording the X-displacement. The observation operator for such a setup takes the following simple form,
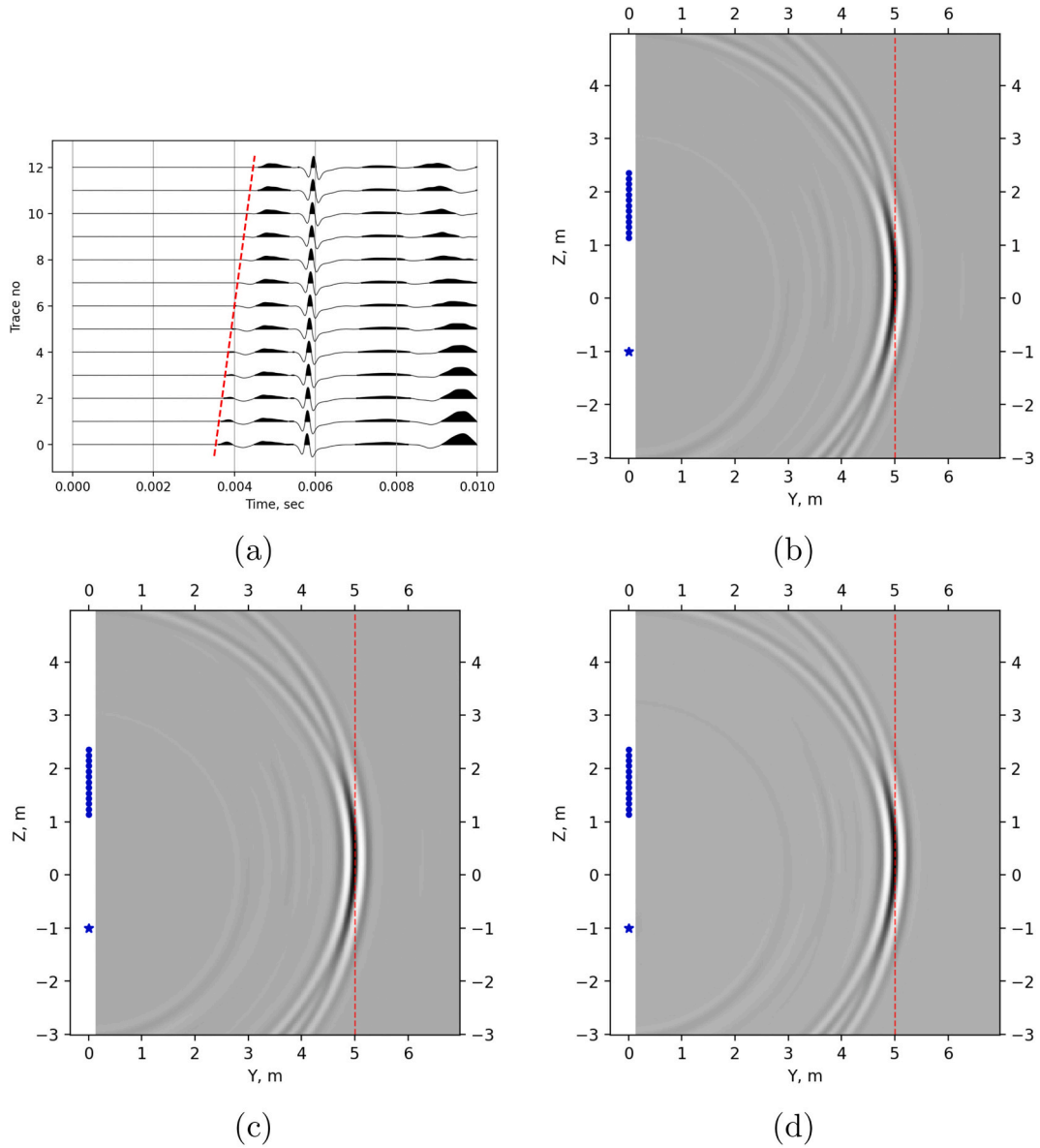
Fig. 9. Test 2. ED-EM of SH reflections: (a) data shot with the first arrivals muted and the sign of wiggles inverted, (b) image with the strain IC I_μ, (c) image with the deviator IC I'_μ, and (d) image with the curl IC I'_μ.

$$d_i(t) = Q_i \boldsymbol{u} := \int_{V_s} u_x\left(t, \boldsymbol{x}\right) \delta(\boldsymbol{x} - \boldsymbol{x}_i)\, d\boldsymbol{x}. \tag{33}$$

Fig. 8 shows images obtained with the I_ρ and I_λ ICs. The single-shot images in Fig. 8(b), (c), referred to as "banana-doughnut kernels" by Tromp et al. (2005), offer valuable insights into the capabilities of RTM in terms of sensitivity and spatial resolution. Apparently, I_ρ generated two shallow spurious interfaces due to the PS-reflection.

6.2. Test 2: Shear-modulus imaging conditions

This test focused on assessing the three shear-modulus ICs. The computation is performed in the ED-EM scenario. As before, the geological model consists of material 1 and material 2. The vertical interface is placed in the plane $y = 5m$ to maximize the SH response. No processing to the synthetic data is applied apart from muting. The calculation was performed with the tool consisting of 13 circular arrays

of receivers separated 0.1016 m apart; the distance between the source and the first receiver was 2.1336 m. The source emitted the 3 kHz Ricker wavelet (Fig. 9).

Fig. 9 displays the images obtained from the experiment. All the images exhibit similarity. Evidently, elastic RTM applied to elastic data yields accurate reflector images, in contrast to the fluid-solid case, as discussed below.

6.3. Test 3: Impact of the borehole

This test evaluates the extent to which the presence of the borehole influences the imaging results. We introduce a fluid-filled borehole into the geological model (Table 1) and consider FSD-EM and FSD-EM scenarios. For the FSD-EM approach, the data consists of pressure readings from circular arrays, which undergo dipole processing (2). The borehole significantly affects the data, transforming the reflection from a compact pulse into a long wave train with an extended tail and a higher frequency
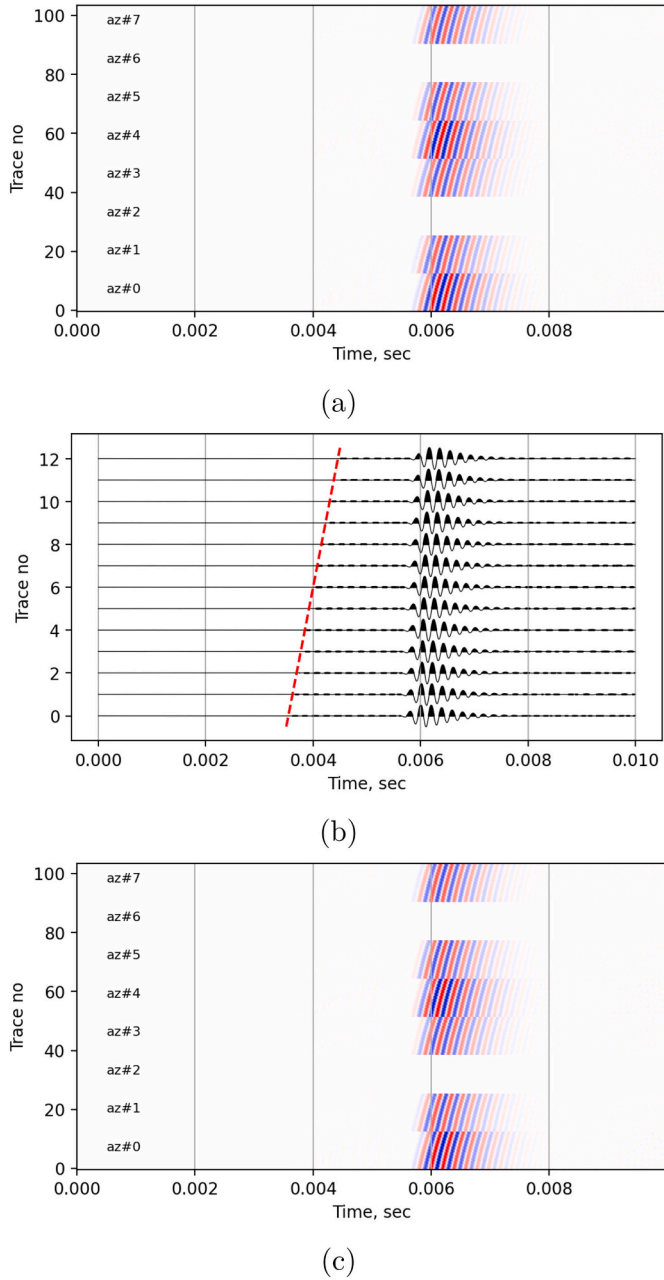
Fig. 10. Test 3. Processing of fluid-solid data: (a) muted synthetic data $\boldsymbol{d}(t)$, (b) processed data $\boldsymbol{g}(t)$, (c) adjoint source function $\boldsymbol{q}$.

content. In the FSD-EM approach, we fed the processed data into the elastic RTM engine.

The FSD-FSM requires modifying how the processed data are injected into the adjoint source. Let $\boldsymbol{d}(t)$ be a time-dependent data vector with dimensions equal to the total number of receivers K, counting N_z circular arrays and N_a azimuthal receivers per array. In this case, $N_z = 13$, $N_a = 8$, $K = 104$. Thus,

$$\boldsymbol{g}(t) = \boldsymbol{Pd}(t) = PQ\varphi(t), \tag{34}$$

where $\boldsymbol{g}(t)$ is the XX processed data, $Q : H^1(V_f) \to \mathbb{R}^K$ is a vector-valued restriction operator whose components described by (13). The pro-

cessing operator $P \in \mathbb{R}^{N_z \times K}$ acts according to (2). Obviously, on the right-hand side of the adjoint problem (19), we will have

$$\boldsymbol{q}(t) = Q^* P^* \boldsymbol{d}(t) \tag{35}$$

instead of just $Q^* \boldsymbol{d}(t)$. We dropped the time derivative in the definition of the operator Q^* to avoid differentiating the field data — more on that in the next section.

Fig. 10 illustrates the data processing relative to the FSD-FSM mode. Panel (a) shows the row data, as would be recorded by a tool. Panel (b) depicts the data after standard dipole processing. Panel (c) illustrates processed data injected into the adjoint sources.

The comparison of the ED-EM, FSD-EM, and FSD-FSM modes is presented in Fig. 11. The elastic RTM of solid data results in the intense ringing of the signal, with the reflector image being radially extended by a lengthy tail. It is also apparent that the azimuthal resolution of the sonic data is inherently low, as evident from slices perpendicular Z-axis, see Fig. 11, the middle column.

Surprisingly, the fluid-solid RTM does not recover a compact reflection but produces even stronger ringing. The only positive aspect of FSD-FSM over FSD-EM is that the former resulted in a more symmetric reflector image. Currently, the reasons behind it are not fully understood. On the one hand, applying various filters or LS-RTM may improve the performance of the FSD-FSM approach. However, it may also be the case that the necessary information to build compact reflector images is inherently absent in sonic data, notorious for their narrow aperture.

### 6.4. Test 4. Effect of time differentiation

According to Eq. (35), the processed data require differentiation. Fig. 12(a) compares the XX dipole data and their corresponding time derivative. The differentiation process was implemented as low-pass filtering, Fourier transform, phase shift, and inverse Fourier transform to enhance the algorithm's stability. It can be observed that the differentiation mainly resulted in a phase shift of half a cycle. As a result, the imaging results obtained from the differentiated and non-differentiated data were essentially the same, exhibiting a half-cycle phase shift, see Fig. 12(b), (c).

7. Field data tests

This section discusses tests conducted with real data utilizing V100 GPUs. We selected a data set recorded within an open borehole using a tool equipped with a pair of dipole sources and 13 groups of receivers, each containing eight azimuthal receivers. The distances between the source and the first group, and between subsequent groups, were 2.5908 m and 0.1524 m, respectively, with a tool step along the borehole of 0.1524 m.

Initially, we generated synthetic seimograms using a reduced record lengh of 15 ms. The elastic medium comprised two half-spaces separated by a boundary sloping at a 10° angle. The maximum distance from the well to the boundary was 15 m. The parameters of the half-spaces are given in Table 2.

Fig. 13 shows one seismogram for eight azimuths, and the resulting XX seismogram after dipole processing. Dispersive tube waves are evident up to approximately 7 ms, while reflections become apparent around 10.7 ms. All 256 seismograms are depicted in Fig. 14. We computed XX dipole seismograms and muted the initial 7 ms. Elastic migration in a homogeneous medium with velocities of 6 km/s and 3 km/s was applied (i.e. the fluid column was replaced with the solid). The curl-curl IC was utilized to generate the image, with the final results presented in Fig. 15. The primary challenge affecting image quality is
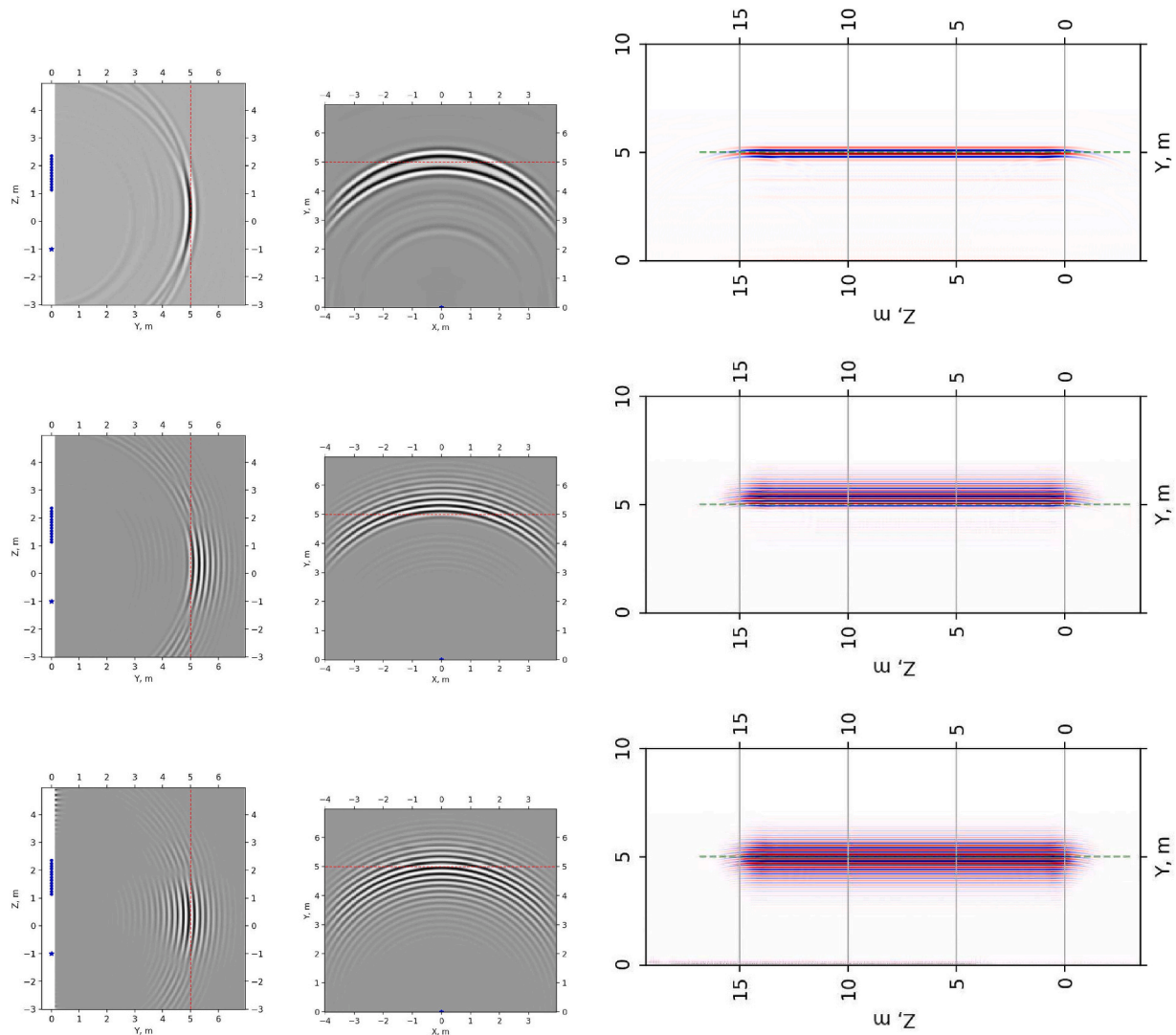
Fig. 11. Test 3. Impact of the borehole on imaging results: ED-EM (top row), FSD-EM (middle row), FSD-FSM (bottom row). Left and middle columns: a single shot image in two projections, right column: 100 shot image. The borehole impact manifests itself as blurred images of reflectors in both the FSD-EM and FSD-FSM images.
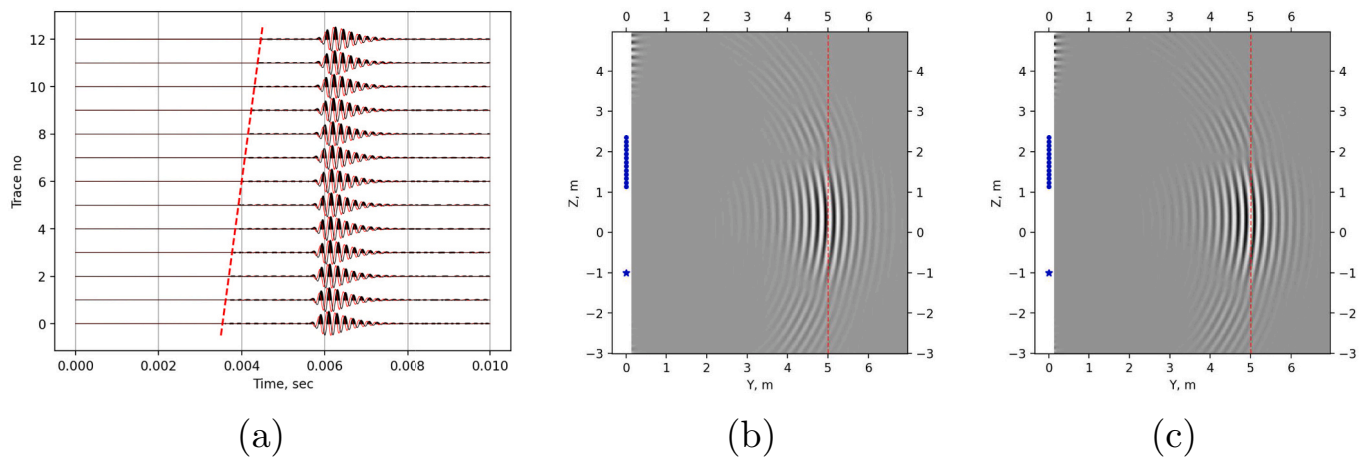

Fig. 12. Test 4. Effect of time differentiation: (a) comparison of processed data (black) with their time derivatives (red), (b) image w/out time differentiation, (c) image with time differentiation. (For interpretation of the references to colour in this figure legend, the reader is referred to the web version of this article.)

Table 2

Material properties used to simulate 256 synthetic seismograms.

	ρ, kg/m^3	V_p, m/s	V_s, m/s
Water	1000	1500	
Material 1	2600	6000	3000
Material 2	2600	5900	2900
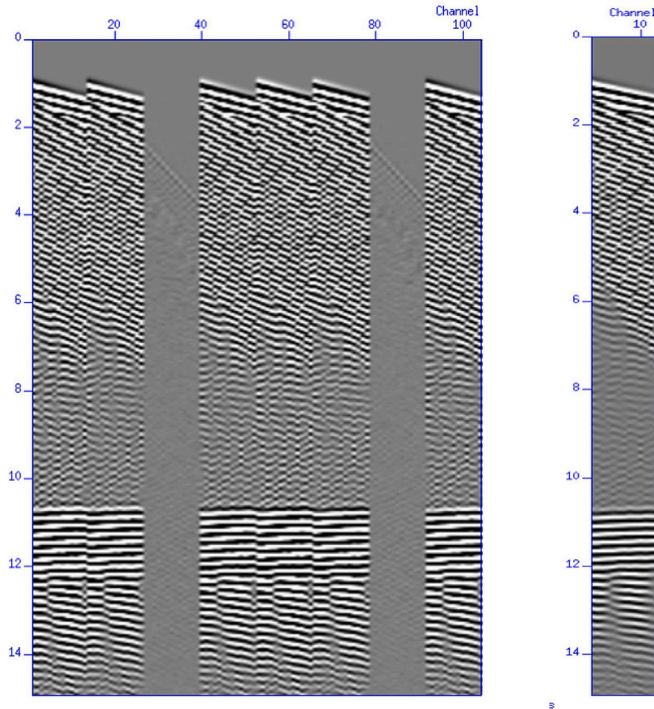
Fig. 13. Simulated 15 ms seismogram. The left panel displays eight azimuthal seismograms, each separated by 45°, with 13 channels seismograms. The right panel shows the XX seismogram after dipole processing. In both panels, the vertical axis represents time in milliseconds. Reflected wave train is visible at 10.7 s.

reverberation in the fluid column, resulting in the boundary appearing as a series of reflections.

The algorithm was then tested on a small set of field data consisting of seismograms recorded by a tool with the same geometric dimensions as previously specified. Each record had a length of 40 ms. Before analysis, the data underwent several preprocessing steps, including forming the dipole dataset, high-pass filtering, and removing tube waves, as outlined in Alqatari et al. (2021). A total of 392 seismograms were utilized, covering approximately a 60 m interval along the well. For the RTM velocity model we employed smoothed 1D logs (we do not have permission to publish them), but observed minimal impact on the images compared to the averaged homogeneous model — likely due to the short data section used. The original data and the resulting migrated images are depicted in Fig. 16. On the migrated section, three known geological horizons are visible, indicated by yellow arrows. These boundaries align with those identified from the same data using 2D acoustic RTM, as reported by Alqatari et al. (2021). We do not have permission to disclose further geological details or directly compare the two sets of images.

8. Discussion

In this section, we discuss several properties of SEM sonic RTM that are significant from the geophysical perspective.

The lack of 3D velocity models is a fundamental limitation for single-well sonic RTM. The survey is aligned along a borehole which is unfavorable for the FWI velocity model building. In practice, the only velocity information available comes from classical sonic logging, which is essentially 1D. Therefore, even though our 3D SEM engine utilizes a 3D model internally, this feature has not proven to be a practical game-changer.

The 3D SEM sonic modelling offers superior accuracy and speed compared to FD methods, as demonstrated in multiple occasions. This advantage primarily stems from SEM's ability to accurately represent curved borehole geometries and effectively simulate fluid-solid coupling. Consequently, it was anticipated that 3D fluid-solid SEM migration would yield high-quality images by effectively separating P-waves, S-waves, and converted wave reflections due to the specific imaging conditions, and migrating recorded wave trains into shorter, more distinct reflectors. However, in the limited examples analyzed so far, we have not observed a significant improvement in image quality compared to the acoustic 2D images published in Alqatari et al. (2021) (we do not have permission to publish the comparision at the time of writing).

We attribute the lack of noticeable improvement to several factors. First, due to the small aperture in deep sonic setups, the majority of information is derived from travel time. Simpler tools (2D acoustic RTM, Kirchhoff migrations etc.), provide a faster means of migrating a (ringing) event in the seismogram to a (ringing) event in the image. Second, in the dipole-dipole sonic setup, S-waves dominate other wave types. Although there might be situations where converted waves could degrade image quality, making elastic RTM potentially useful for noise removal, this factor has not proven as significant as expected. Finally, the introduction of the borehole into straightforward RTM framework did not eliminate the ringing noise as anticipated.

Given that SEM RTM is time-consuming and requires substantial programming efforts, we have concluded that for conventional deep sonic imaging, it is unlikely to offer significant advantages over simpler methods. However, there are several research directions where SEM modelling remains essential. One area is addressing reverberation noise in deep sonic imaging. Potential solutions include the matched filter approach proposed by Hirabayashi et al. (2022) or accounting for non-linearity of the imaging operator. Both methods require accurate borehole simulation, making SEM crucial in this context. Another direction is shallow sonic imaging. The fundamental challenge in this area is the presence of strong tube waves masking incoming reflections. SEM simulation is particularly well-suited to study this issue.

9. Conclusions

We have examined the 3D fluid-solid RTM of dipole sonic data. It is based on the SEM that enables accurate computation of field data in the purely elastic or fluid-solid regime. This study involved the implementation of sonic solid-fluid RTM code on a GPU, marking a novel achievement.

Our approach to sonic RTM revolves around several key elements. Firstly, we employ small, independent computational grids for each shot. Second, use high-order elements, reducing the size of the computational problem and improving fine-grained parallelism. Third, the multiplication of the local stiffness tensor with a local vector of displacements is performed in a thread block's shared memory. Finally, we proposed a strategy for grid generation, specifically designed to construct a mesh around a borehole with a small element count.

We reviewed three shear-modulus imaging conditions and subject them to numerical testing. It has been found that these conditions generate almost identical images, with the curl-curl condition being the most economical. We present several tests using synthetic data and a small real data set, primarily serving as a validation test for our software. However, these experiments also highlight important aspects of sonic
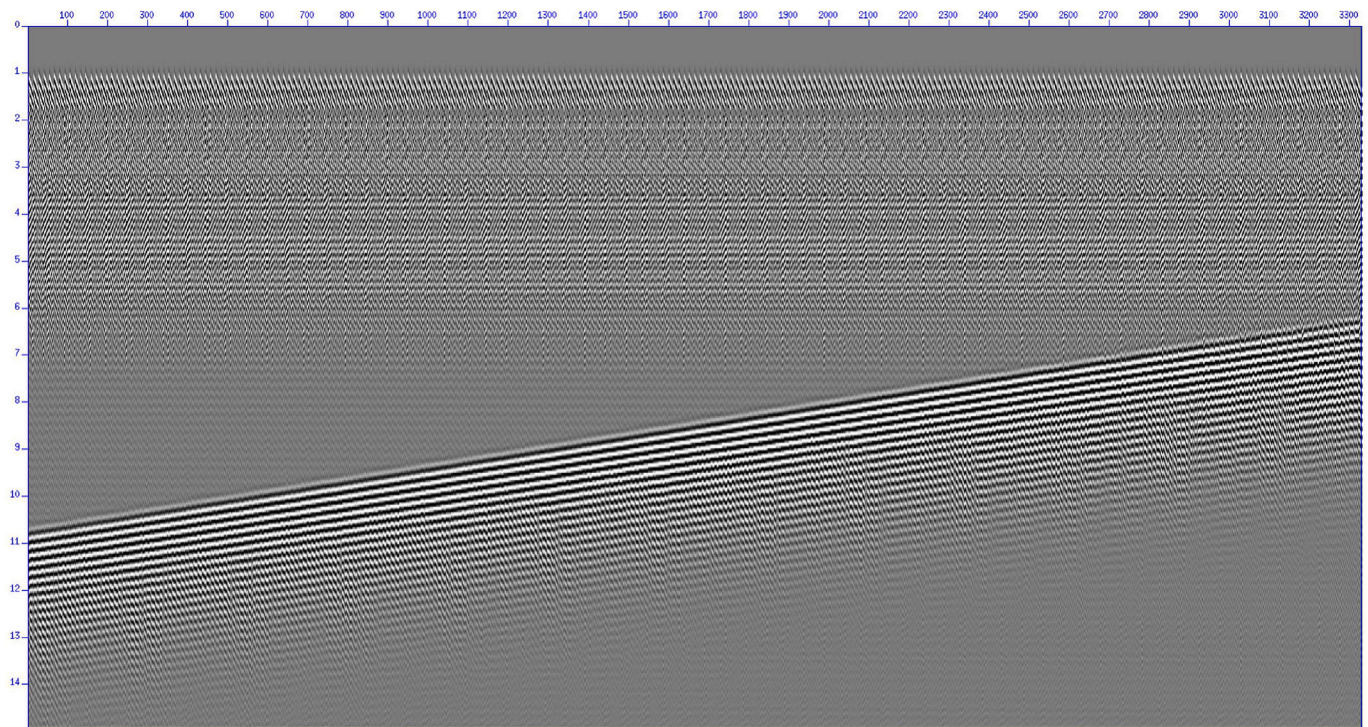
Fig. 14. Simulated 15 ms seismograms. The panel presents 256 seismograms arranged side-by-side, each containing 8 azimuthal receiver arrays with 13 channels per array. The vertical axis represents time in milliseconds, while the horizontal axis indicates the channel number. A time-dependent gain is applied to enhance visibility of the incoming reflected wave train, which starts at 10.8 ms on the left side and 6 ms on the right side.
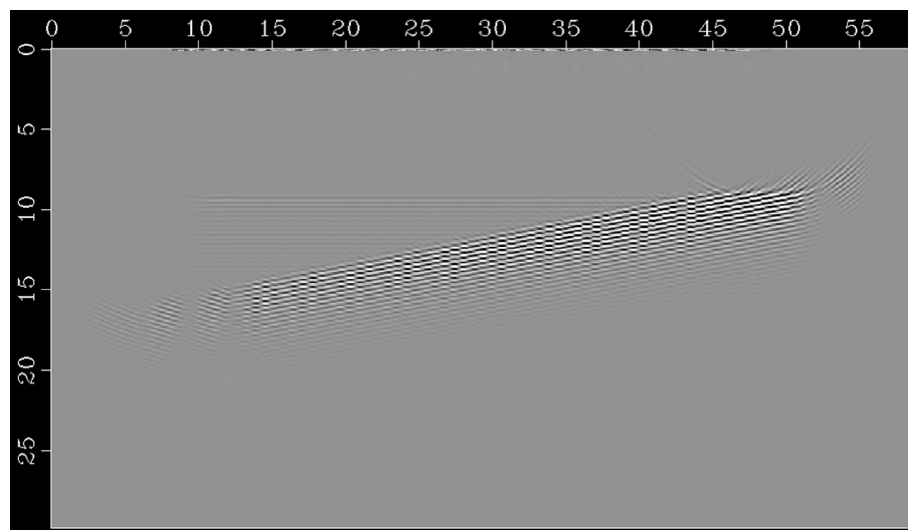
Fig. 15. Image obtained after migrating 256 synthetic seismograms. The X-axis represents radial distance in meters, while the Y-axis displays distance along the borehole in meters.

RTM, notably the significant impact of reverberation noise from the borehole.

While further research and efforts are necessary, our results indicate that the sonic community already possesses the technical capability to perform industrial-scale sonic RTM, particularly with top-tier multi-GPU clusters, equipped with with modern cards, such as A100, or H100, each featuring 80GB of memory.

CRediT authorship contribution statement

Mikhail Malovichko: Writing – original draft, Visualization, Software, Investigation, Formal analysis, Data curation, Conceptualization. **Denis Sabitov:** Software. **Maxim Dmitriev:** Validation, Software, Resources. **Timur Zharnikov:** Project administration.
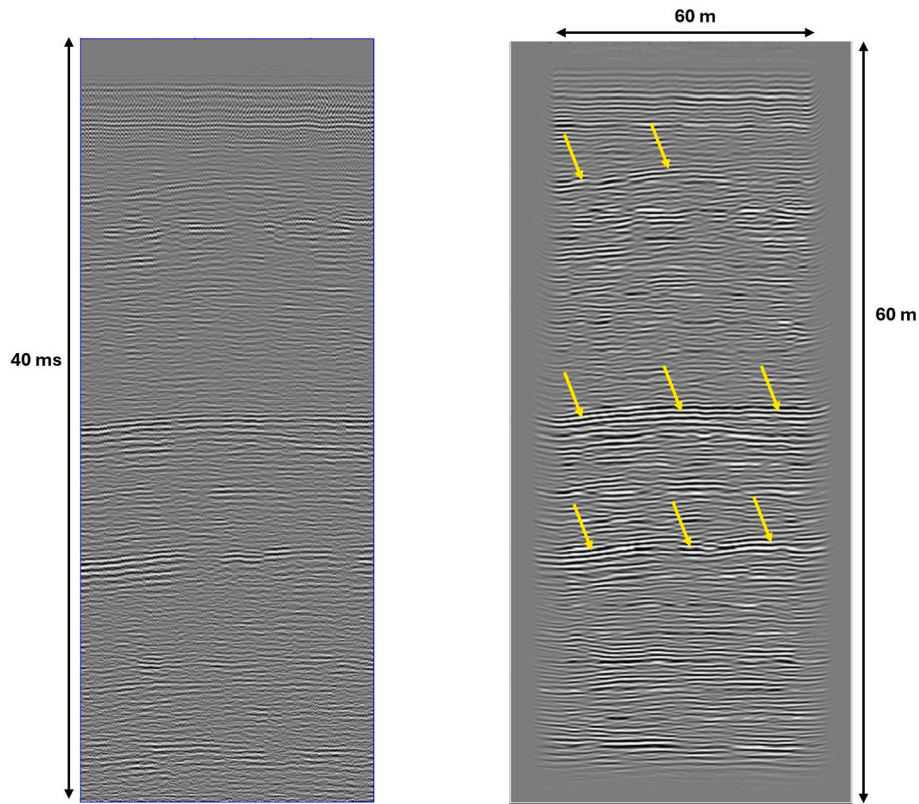
Fig. 16. Real data and migrated section. Left: processed 40-ms real seismograms. Right: migrated image.

Declaration of competing interest

The authors declare that they have no known competing financial interests or personal relationships that could have appeared to influence the work reported in this paper.

Appendix A. GPU tensor reduction

In this section, we consider a GPU implementation of the SEM method. We apply the standard Newmark scheme, which can be found everywhere. One possible form of the scheme is the following,

$$
\begin{aligned}
A &= M^{-1}(F - SU^n), \\
V^{n+1} &= V^n + \tau A, \\
U^{n+1} &= U^n + \tau V^n + A\tau^2/2,
\end{aligned}
\tag{A1}
$$

where M is the global mass matrix, S is the global stiffness matrix, τ is the time step, F, U and V are global load vector, vector of displacement DOFs, and vector of velocity DOFs, respectively. Most of the computational time is spent on the matrix-vector multiplication (tensor reduction) Su^n in the solid region because the number of fluid elements is typically small. It has been pointed out many times that SU^n must be implemented in each element independently to exploit GPU parallelism. Still, this operation dominates computations, so we review it in more detail.

Let us consider a given solid element K, which contains N^3 integration points indexed as $\{k, l, m\}$. Here and below, we assume that $k,l,m \in [1, N]$. Let u_p^{klm} be a 4-dimensional vector containing N^3 three-dimensional DOFs with index $p = 1, 2, 3$ corresponding to the vector component. In this section, we use subscripts and superscripts solely to simplify notation, not for contravariant and covariant tensor properties.

Let us denote the local stiffness matrix S (not to be confused with the global matrix). It is given by

$$
S = \int_K \nabla^T \overleftarrow{\mathscr{L}}^{abc}(x,y,z) : \widehat{C} : \nabla \overleftarrow{\mathscr{L}}^{klm}(x,y,z) \, dV.
\tag{A2}
$$

"Matrix" S is, in fact, a multi-dimensional array because both the test and trial spaces are indexed with the indices of a GLL point and components of a 3D vector. Quantity $\overleftarrow{\mathscr{L}}^{klm}$ is a local basis function, which is a tensor product of the basis polynomials. The arrow $\rightarrow$ denotes a three-dimensional vector in this section. We want to compute the "matrix-vector" product

$$
w = S \otimes u.
\tag{A3}
$$

Our algorithm is organized in several steps.

- **Step 1.** Compute displacement derivatives of the reference element.

  The derivatives are given according to the formulas,

$$\frac{\partial \overleftarrow{u}}{\partial r}(r_k, s_l, t_m) = \sum_{\alpha=1}^{N} \ell'_\alpha(r_k) \overleftarrow{u}(r_\alpha, s_l, t_m),$$

$$\frac{\partial \overleftarrow{u}}{\partial s}(r_k, s_l, t_m) = \sum_{\alpha=1}^{N} \ell'_\alpha(s_l) \overleftarrow{u}(r_k, s_\alpha, t_m),$$ (A4)

$$\frac{\partial \overleftarrow{u}}{\partial t}(r_k, s_l, t_m) = \sum_{\alpha=1}^{N} \ell'_\alpha(t_m) \overleftarrow{u}(r_k, s_l, t_\alpha).$$

Here $\ell'(x)$ denotes the derivative of a given basis function $\ell(x)$.

In the code, this is performed by the following array manipulations,

$$e_{p1}^{klm} = \sum_{\alpha=1}^{N} M_{k\alpha} u_p^{\alpha lm}, \quad p = 1, 2, 3,$$

$$e_{p2}^{klm} = \sum_{\alpha=1}^{N} M_{l\alpha} u_p^{k\alpha m}, \quad p = 1, 2, 3,$$ (A5)

$$e_{p3}^{klm} = \sum_{\alpha=1}^{N} M_{m\alpha} u_p^{kl\alpha}, \quad p = 1, 2, 3.$$

Here $e_{pq}^{klm} with p, q \in \{1, 2, 3\}$ is a 5-dimensional array of displacement derivatives (nine values per GLL point), M is a matrix containing derivatives of the basis polynomials at GLL points,

$$M_{ij} = \ell'_j(x_i)$$ (A6)

- **Step 2.** Compute inverse Jacobian.

  The Jacobian is a map $\{r_k, s_l, t_m\} \mapsto \{x_k, y_l, z_m\}$, which cab be represented as the following matrix,

$$J = \begin{bmatrix} \partial x/\partial r & \partial x/\partial s & \partial x/\partial t \\ \partial y/\partial r & \partial y/\partial s & \partial y/\partial t \\ \partial z/\partial r & \partial z/\partial s & \partial z/\partial t \end{bmatrix}$$ (A7)

The inverse Jacobian is a map $\{x_k, y_l, z_m\} \mapsto \{r_k, s_l, t_m\}$,

$$J^{-1} = \begin{bmatrix} \partial r/\partial x & \partial r/\partial y & \partial r/\partial z \\ \partial s/\partial x & \partial s/\partial y & \partial s/\partial z \\ \partial t/\partial x & \partial t/\partial y & \partial t/\partial z \end{bmatrix}$$ (A8)

For a given physical point $\overleftarrow{P}^{klm} = (x_k, y_l, z_m)$ and reference point $\overleftarrow{Q}^{klm} = (r_k, s_l, t_m)$, elements of the Jacobian can be represented as follows,

$$\frac{\partial \overleftarrow{P}}{\partial r}(x_k, y_l, z_m) = \sum_{\alpha=1}^{N} \ell'_\alpha(r_k) \overleftarrow{P}^{\alpha lm},$$

$$\frac{\partial \overleftarrow{P}}{\partial s}(x_k, y_l, z_m) = \sum_{\alpha=1}^{N} \ell'_\alpha(s_l) \overleftarrow{P}^{k\alpha m},$$ (A9)

$$\frac{\partial \overleftarrow{P}}{\partial t}(x_k, y_l, z_m) = \sum_{\alpha=1}^{N} \ell'_\alpha(t_m) \overleftarrow{P}^{kl\alpha}.$$

In the code this is represented with the following array manipulations,

$$J_{p1}^{klm} = \sum_{\alpha=1}^{N} M_{k\alpha} P_p^{\alpha lm}, \quad p = 1, 2, 3,$$

$$J_{p2}^{klm} = \sum_{\alpha=1}^{N} M_{l\alpha} P_p^{k\alpha m}, \quad p = 1, 2, 3,$$ (A10)

$$J_{p2}^{klm} = \sum_{\alpha=1}^{N} M_{m\alpha} P_p^{kl\alpha}, \quad p = 1, 2, 3.$$

As soon as J^{klm} is available, $(J^{-1})^{klm}$ is computed by inverting the 3-by-3 matrix.

- **Step 3.** Compute displacement derivatives in the physical element.

  Here we pre-multiply $\overleftarrow{u}$ with J^{-T}, e.g.

$$\frac{\partial \overleftarrow{u}}{\partial x} = \frac{\partial \overleftarrow{u}}{\partial r}\frac{\partial r}{\partial x} + \frac{\partial \overleftarrow{u}}{\partial s}\frac{\partial s}{\partial x} + \frac{\partial \overleftarrow{u}}{\partial t}\frac{\partial t}{\partial x}. \tag{A11}$$

It can be formally expressed as following array operations,

$$g_{p1}^{klm} = \sum_{\alpha=1}^{3} \left(J^{-1}\right)_{1\alpha}^{klm} e_{p\alpha}^{klm}, p = 1, 2, 3,$$

$$g_{p2}^{klm} = \sum_{\alpha=1}^{3} \left(J^{-1}\right)_{2\alpha}^{klm} e_{p\alpha}^{klm}, p = 1, 2, 3, \tag{A12}$$

$$g_{p3}^{klm} = \sum_{\alpha=1}^{3} \left(J^{-1}\right)_{3\alpha}^{klm} e_{p\alpha}^{klm}, p = 1, 2, 3,$$

where array g contains 9 displacement derivatives at each of N^3 GLL points. In practice, we compute 6 unique components of the strain tensor.

- **Step 4.** Compute the stress tensor and multiply it by quadratire weights.
  Formally we write

$$\sigma_{ij}^{klm} = \left(\sum_{\alpha=1}^{3} \sum_{\beta=1}^{3} c_{ij\alpha\beta}^{klm} g_{\alpha\beta}^{klm}\right) w_{klm}, \tag{A13}$$

where w_{klm} are the quadrature weights. In the code, however, we compute six unique stress tensor components using the strain tensor from the previous step. Therefore, this step's work is minimal, especially if the solid is isotropic.

- **Steps 5.** Apply operator J^{-1}.
- **Steps 6.** Apply operator M^T.
  Overall, we have the following formal representation for the element stiffness matrix,

$$S = M^T \otimes J^{-1} \otimes C \otimes J^{-T} \otimes M \tag{A14}$$

The most expensive parts are Jacobian computation (Step 1) and displacement derivative computations (Steps 2 and 6), involving intensive computations and irregular access to large chunks of memory. Fig. 17 illustrates the access pattern. Our GPU mitigates the related overburden using the GPU's shared memory, as described below.

Global DOFs for U and V, as well as the coordinates of the GLL points, are stored in the global GPU memory. The primary time loop launches a grid of thread blocks with the block size N^3, so within each thread block, each thread corresponds to a single local DOF. The threads copy N^3 coordinates to a shared-memory array P and N^3 DOFs of displacement into a shared-memory array U. For example, for $N = 8$ and the single-precision arithmetic, each array has a size of $3 \times 512 \times 4 \approx 6kB$. Having array P copied, each thread computes Step 1 as described above. Steps 2 and 6 are performed similarly: each thread performs computations in the shared memory using the same access pattern. This scheme offers a drastic improvement over uncoalesced irregular access to the global memory, though it still introduces the bank conflict in the shared memory.
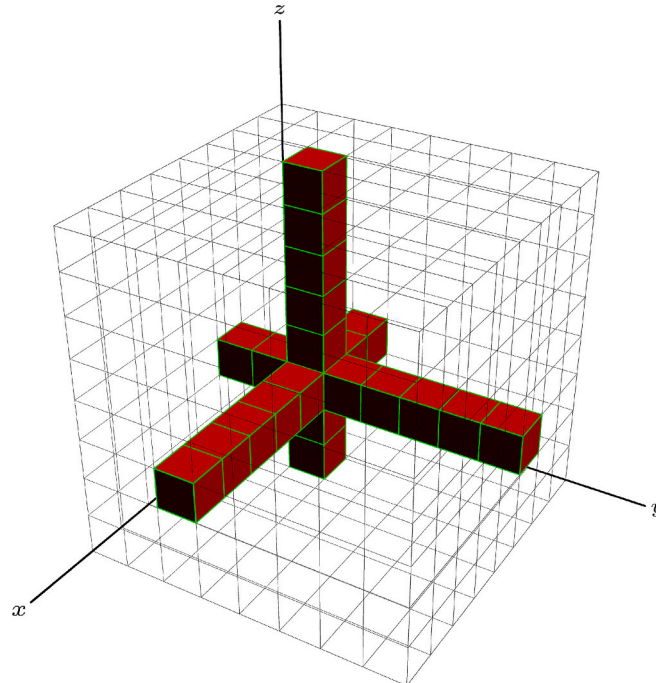

Fig. 17. Access pattern for a thread $k = l = m = 2$ within a thread block $8 \times 8 \times 8$.

Data availability

The data that has been used is confidential.

References

Alqatari, H., Tonellot, T.-L., Mubarak, M., 2021. Near-borehole imaging using full-waveform sonic data, SPE-204765-MS. SPE Middle East Oil & Gas Show and Conference.

Baysal, E., Kosloff, D.D., Sherwood, J.W.C., 1983. Reverse time migration. Geophysics 48 (11), 1514–1524. https://doi.org/10.1190/1.1441434.

Bazulin, M., Sabitov, D., Charara, M., 2021. Determination of the elastic parameters of a VTI medium from sonic logging data using deep learning. Comput. Geosci. 152, 104759. https://doi.org/10.1016/j.cageo.2021.104759. ISSN 0098-3004.

Bolshakov, A., Patterson, D., Lan, C., 2011. Deep Fracture Imaging around the Wellbore Using Dipole Acoustic Logging. SPE Annual Technical Conference and Exhibition held.

Byun, J., Toksöz, M.N., 2006. Effects of an off-centered tool on dipole and quadrupole logging. Geophysics 71 (4), F91–F100. https://doi.org/10.1190/1.2217368.

Cao, J., Brossier, R., Metivier, L., 2021. 3D Fluid-Solid Coupled Full-Waveform Inversion for Ocean-Bottom Seismic Data.

Chabot, L., Henley, D., Brown, R., Bancroft, J., 2001. Single-well seismic imaging using the full waveform of an acoustic sonic. CREWES Res. Report 13.

Chaljub, E., Capdeville, Y., Vilotte, J.-P., 2003. Solving elastodynamics in a fluid–solid heterogeneous sphere: a parallel spectral element approximation on non-conforming grids. J. Comput. Phys. 187 (2), 457–491. https://doi.org/10.1016/S0021-9991(03)00119-0. URL. ISSN 0021-9991. https://www.sciencedirect.com/science/article/pii/S0021999103001190.

Chang, W., McMechan, G.A., 1987. Elastic reverse-time migration. Geophysics 52 (10), 1365–1375. https://doi.org/10.1190/1.1442249.

Cheng, A.C.H., Blanch, J.O., 2008. Numerical modeling of elastic wave propagation in a fluid-filled borehole. Commun. Comput. Phys. 3 (1), 33–51.

Cheng, C.H., Toksöz, M.N., 1981. Elastic wave propagation in a fluid-filled borehole and synthetic acoustic logs. Geophysics 46 (7), 1042–1053. https://doi.org/10.1190/1.1441242.

Cheng, N., Cheng, C.H., Toksöz, M.N., 1995. Borehole wave propagation in three dimensions. J. Acoust. Soc. Am. 97 (6), 3483–3493. https://doi.org/10.1121/1.412996.

Coates, R., Kane, M., Chang, C., Esmersoy, C., Fukuhara, M., Yamamoto, H., 2000. SPE-65457-MS, Single-well sonic imaging: high-definition reservoir cross-sections from horizontal. SPE/CIM International Conference on Horizontal Well Technology.

Feng, Z., Schuster, G.T., 2017. Elastic least-squares reverse time migration. Geophysics 82 (2), S143–S157. https://doi.org/10.1190/geo2016-0254.1.

Festa, G., Vilotte, J.-P., 2005. The Newmark scheme as velocity–stress time-staggering: an efficient PML implementation for spectral element simulations of elastodynamics. Geophys. J. Int. 161 (3), 789–812. https://doi.org/10.1111/j.1365-246X.2005.02601.x.

Fortin, J., Rehbinder, N., Staron, P., 1991. Reflection imaging around a well with the EVA full waveform tool. Log Analyst 32 (3), 271–278.

Gong, H., Chen, H., He, X., Wang, X., 2015. Eliminating the azimuth ambiguity in single-well imaging using 3c sonic data. Geophysics 80 (1), A13–A17. https://doi.org/10.1190/geo2014-0337.1.

Gong, H., Cheng, H., He, X., Su, C., Wang, X., 2016. Utilization of a Combined Monopole-Dipole Measurement Mode for Improved Single-Well Imaging Method. SEG Technical Program Expanded Abstracts.

Gong, H., Chen, H., He, X., Su, C., Wang, X.-M., Wang, B.-C., Yan, X.-H., 2018. Modeling and inversions of acoustic reflection logging imaging using the combined monopole–dipole measurement mode. Appl. Geophys. 15, 393–400.

Grohmann, M., Niederleithinger, E., Büttner, C., Buske, S., 2024. Application of iterative elastic reverse time migration to shear horizontal ultrasonic echo data obtained at a concrete step specimen. Near Surface Geophys. https://doi.org/10.1002/nsg.12318.

Haldorsen, J., 2005. Borehole Sonic Data Processing Method. US Patent 6956790B2.

Hirabayashi, N., 2016. Reflector imaging using trial reflector and crosscorrelation: Application to fracture imaging for sonic data. Geophysics 81 (6), S433–S446.

Hirabayashi, N., Sakiyama, N., Ikegami, T., 2017. Characteristics of waveforms recorded by azimuthally spaced hydrophones of sonic logging tool for incident plane waves. Geophysics 82 (6), D353–D368. https://doi.org/10.1190/geo2017-0201.1.

Hirabayashi, N., Dahlhaus, L., Kumar, R., Karpekin, Y., 2022. Matched filter for s-wave sonic imaging. Geophysics 87 (4), 137–D146. https://doi.org/10.1190/GEO2021-0547.1.

Hornby, B., Bacciarelli, M., Ospina, R., Assous, S., 2024. Reflection Sonic Imaging Using Slim-Hole Pipe Conveyed Sonic Tools,SPWLA-2024-0081, SPWLA 65th. Annual Logging. https://doi.org/10.30632/SPWLA-2024-0081.

Hornby, B., Peterman, P., Hager, C., Draucker, A., Bolshakov, A., 2018. Reflection Sonic Imaging of Complex near-Borehole Structure in Slow Formations. SEG International Exposition and Annual Meeting.

Hornby, B.E., 1989. Imaging near-borehole of formation structure using full-waveform sonic data. Geophysics 54 (6), 747–757.

Hornby, B.E., Wiggins, R., 1989. Borehole Logging Methods for Detection and Imaging of Formation Structural Features. US patent, 4817059.

Karpekin, Y., Orlova, S., Tukhtaev, R., Ovchinnikov, A., Kuntsevich, V., 2019. SPE-196958-MS. Borehole acoustic reflection survey in horizontal wells: High resolution reservoir structure to guide properties distribution. SPE Russian Petroleum Technology Conference.

Komatitsch, D., Tromp, J., 1999. Introduction to the spectral element method for three-dimensional seismic wave propagation. Geophys. J. Int. 139 (3), 806–822.

Komatitsch, D., Vilotte, J.-P., 1998. The spectral element method: an efficient tool to simulate the seismic response of 2D and 3D geological structures. Bull. Seismol. Soc. Am. 88 (2), 368–392.

Komatitsch, D., Barnes, C., Tromp, J., 2000. Wave propagation near a fluid-solid interface: a spectral-element approach. Geophysics 65 (2), 623–631.

Landau, L.D., Lifshitz, E.M., 1959. Fluid Mechanics. Pergamon Press, Addison-Wesley.

Li, D., Tian, X., Hu, H., Tang, X.-M., Fang, X., Zheng, Y., 2020. Gaussian beam imaging of fractures near the wellbore using sonic logging tools after removing dispersive borehole waves. Geophysics 85 (4), D133–D143. https://doi.org/10.1190/geo2019-0104.1.

Li, J., Tao, G., Zhang, K., Wang, H., 2013a. Application of the Reverse Time Migration in Acoustic Reflection Imaging Logging. EAGE Extended Abstracts.

Li, J., Tao, G., Zhang, K., Ye, Q., 2013b. Borehole Sonic Reflection Imaging by Finite Difference Reverse Time Migration. SEG Houston 2013 Annual Meeting.

Li, J., Tao, G., Zhang, K., Wang, B., Wang, H., 2014. An effective data processing flow for the acoustic reflection image logging. Geophys. Prospect. 62, 530–539.

Li, J., Innanen, K.A., Tau, G., Lines, L., 2016. Resolving Azimuthal Ambiguity in Borehole Imaging Using a 3D Borehole RTM Scheme. SEG International Exposition and 86th Annual Meeting.

Li, J., Innanen, K., Wang, B., Tao, G., 2019. Azimuth ambiguity elimination for borehole imaging using 3D borehole RTM scheme. J. Appl. Geophys. 163, 103–111.

Li, Y.-S., Wu, H.-L., Liu, P., Feng, Z., Wang, K.-W., Zhang, H., Zhang, W.-H., 2024. Research on the differential coefficient least-squares optimization method of reverse time migration in acoustic-reflected S-wave imaging logging. Appl. Geophys. https://doi.org/10.1007/s11770-024-1088-5.

Liu, Q., Tromp, J., 2006. Finite-frequency kernels based on adjoint methods. Bull. Seismol. Soc. Am. 96 (6), 2383–2397.

Luo, Y., Zhu, H., Nissen-Meyer, T., Morency, C., Tromp, J., 2009. Seismic modeling and imaging based upon spectral-element and adjoint methods. Lead. Edge 28 (5), 568–574. https://doi.org/10.1190/1.3124932.

Luo, Y., Tromp, J., Denel, B., Calandra, H., 2013. 3d coupled acoustic-elastic migration with topography and bathymetry based on spectral-element and adjoint methods. Geophysics 78 (4), S193–S202. https://doi.org/10.1190/geo2012-0462.1.

McMechan, G.A., 1983. Migration by extrapolation of time-dependent boundary values. Geophys. Prospect. 31 (3), 413–420.

Meredith, J., 1991. Numerical and Analytical Modelling of Downhole Seismic Sources-the Near and Far Field. PhD thesis. MIT.

Peter, D., Komatitsch, D., Luo, Y., Martin, R., Le Goff, N., Casarotti, E., Le Loher, P., Magnoni, F., Liu, Q., Blitz, C., Nissen-Meyer, T., Basini, P., Tromp, J., 2011. Forward and adjoint simulations of seismic wave propagation on fully unstructured hexahedral meshes. Geophys. J. Int. 186 (2), 721–739. https://doi.org/10.1111/j.1365-246X.2011.05044.x.

Pietroni, N., Campen, M., Sheffer, A., Cherchi, G., Bommes, D., Gao, X., Scateni, R., Ledoux, F., Remacle, J., Livesu, M., 2022. Hex-mesh generation and processing: a survey. ACM Trans. Graph. 42 (2). https://doi.org/10.1145/3554920. ISSN 0730-0301.

Pissarenko, D., Reshetova, G., Tcheverda, V., 2010. 3D finite-difference synthetic acoustic log in cylindrical coordinates. J. Comput. Appl. Math. 234 (6), 1766–1772. https://doi.org/10.1016/j.cam.2009.08.026. ISSN 0377-0427.

Plyushenkov, B.D., Turchaninov, V.I., 2006. Solution of Pride's equations through potentials. Int. J. Modern Phys. 17 (6), 877–908.

Ponomarenko, R., Sabitov, D., Charara, M., 2020. Spectral element simulation of elastic wave propagation through fractures using linear slip model: microfracture detection for CO2 storage. Geophys. J. Int. 223 (3), 1794–1804. https://doi.org/10.1093/gji/ggaa399. ISSN 0956-540X.

Schmitt, D., Tonellot, T., 2020. Wellbore Far-Field Imaging for High Resolution Reservoir Characterization. International Petroleum Technology Conference, Dhahran, Kingdom of Saudi Arabia.

Schmitt, D.P., 1988. Shear wave logging in elastic formations. J. Acoust. Soc. Am. 84 (6), 2215–2229. https://doi.org/10.1121/1.397015.

Schoenberg, M., 1986. Fluid and solid motion in the neighborhood of a fluid-filled borehole due to the passage of a low-frequency elastic plane wave. Geophysics 51 (6), 1191–1205. https://doi.org/10.1190/1.1442174.

Sun, M., Dong, L., Yang, J., Huang, C., Liu, Y., 2018. Elastic least-squares reverse time migration with density variations. Geophysics 83 (6), S533–S547. https://doi.org/10.1190/geo2017-0517.1.

Sun, R., McMechan, G., 1986. Pre-stack reverse-time migration for elastic waves with application to synthetic offset vertical seismic profiles. Proc. IEEE 74 (3), 457–465. https://doi.org/10.1109/PROC.1986.13486.

Sun, R., McMechan, G.A., 2001. Scalar reverse-time depth migration of prestack elastic seismic data. Geophysics 66 (5), 1519–1527. https://doi.org/10.1190/1.1487098.

Tang, X., Cheng, A., 2004. Borehole Acoustics Logging - Theory and Methods. Elsevier, Amsterdam.

Tang, X., Zheng, Y., Patterson, D., 2009. Method for processing reflections in array data to image near-borehole geological structure. US patent 7492664B2.

Tang, X.-M., 2004. Imaging near-borehole structure using directional acoustic-wave measurement. Geophysics 69 (6), 1378–1386. https://doi.org/10.1190/1.1836812.

Tang, X.-M., Patterson, D., 2009. Single-wave S-wave imaging using multicomponent dipole acoustic-log data. Geophysics 74 (6), WCA211–WCA223.

Tang, X.-M., Cao, J.-J., Wei, Z.-T., 2014. Shear wave radiation, reception, and reciprocity of a borehole dipole source: with application to modelling shear-wave reflection survey. Geophysics 79 (2), T43–T50.

Tromp, J., Tape, C., Liu, Q., 2005. Seismic tomography, adjoint methods, time reversal and banana-doughnut kernels. Geophys. J. Int. 160 (1), 195–216. https://doi.org/10.1111/j.1365-246X.2004.02453.x.

Wang, H., Fehler, M., 2017. The wavefield of acoustic logging in a cased hole with a single casing—Part II: a dipole tool. Geophys. J. Int. 212 (2), 1412–1428.

Wang, H., Toksöz, M.N., Fehler, M.C., 2020. Borehole Acoustics Logging - Theory and Methods. Springer, Cham.

Wang, W.-H., Zhang, W., Shi, Y., Ke, X., 2017. Elastic reverse time migration based on wavefield separation. Chin. J. Geophys. 60 (5), 554–568. https://doi.org/10.1002/cjg2.30068.

Wei, Z.-T., Tang, X.-M., 2012. Numerical simulation of radiation, reflection, and reception of elastic waves from a borehole dipole source. Geophysics 77 (6), D253–D261. https://doi.org/10.1190/geo2012-0061.1.

Yan, J., Sava, P., 2008. Isotropic angle-domain elastic reverse-time migration. Geophysics 73 (6), S229–S239. https://doi.org/10.1190/1.2981241.

Zemanek, J., Angona, F., Williams, D., Caldwell, R., 1986. Continuous shear wave logging. In: 25th Annual Logging Symposium Transactions. Society of Professional Well Log Analysts.

Zhang, T., Tao, G., Li, J., Wang, B., Wang, H., 2009. Application of the equivalent offset migration method in acoustic log reflection imaging. Appl. Geophys. 6, 303–310. https://doi.org/10.1007/s11770-009-0041-y.

Zhang, Y., Liu, H., Xiao, H., Zhang, X., Liu, B., Chen, Y., Huang, Z., Liang, C., Wang, W., Wei, G., Sultan, G., Ruiz, E., 2022. Looking Fractures Around the Wellbore: First Successful Azimuthal Dipole Sonic Imaging in a Carbonate Horizontal Well in China, pp. 2977–2984. https://doi.org/10.15530/urtec-2022-3706775.

Zharnikov, T., Sabitov, D., Nikitin, A., 2021. Fast and efficient tool for modelling wellbore far field sonic imaging. In: EAGE Annual 2021. EAGE.

Zhou, H.-W., Hu, H., Zou, Z., Wo, Y., Youn, O., 2018. Reverse time migration: a prospect of seismic imaging methodology. Earth Sci. Rev. 179, 207–227. https://doi.org/10.1016/j.earscirev.2018.02.008. URL. ISSN 0012-8252. https://www.sciencedirect.com/science/article/pii/S0012825217306256.

Zhou, R., Yingping, Li, Xiao-Ming, T., Jackson, J.C., Patterson, D., 2002. Single-Well Imaging with Acoustic Reflection Survey at Mounds, Oklahoma,USA. 64th EAGE Annual Conference and Exhibition.

Zhu, H., Luo, Y., Nissen-Meyer, T., Morency, C., Tromp, J., 2009. Elastic imaging and time-lapse migration based on adjoint methods. Geophysics 74 (6), WCA167–WCA177. https://doi.org/10.1190/1.3261747.